

Compaction Waves in Granular HMX

Los Alamos
NATIONAL LABORATORY

*Los Alamos National Laboratory is operated by the University of California
for the United States Department of Energy under contract W-7405-ENG-36.*

An Affirmative Action/Equal Opportunity Employer

This report was prepared as an account of work sponsored by an agency of the United States Government. Neither The Regents of the University of California, the United States Government nor any agency thereof, nor any of their employees, makes any warranty, express or implied, or assumes any legal liability or responsibility for the accuracy, completeness, or usefulness of any information, apparatus, product, or process disclosed, or represents that its use would not infringe privately owned rights. Reference herein to any specific commercial product, process, or service by trade name, trademark, manufacturer, or otherwise, does not necessarily constitute or imply its endorsement, recommendation, or favoring by The Regents of the University of California, the United States Government, or any agency thereof. The views and opinions of authors expressed herein do not necessarily state or reflect those of The Regents of the University of California, the United States Government, or any agency thereof. Los Alamos National Laboratory strongly supports academic freedom and a researcher's right to publish; as an institution, however, the Laboratory does not endorse the viewpoint of a publication or guarantee its technical correctness.

Compaction Waves in Granular HMX

R. Menikoff

E. Kober

Compaction Waves in Granular HMX

R. Menikoff and E. Kober

Abstract

Piston driven compaction waves in granular HMX are simulated with a two-dimensional continuum mechanics code in which individual grains are resolved. The constitutive properties of the grains are modeled with a hydrostatic pressure and a simple elastic-plastic model for the shear stress. Parameters are chosen to correspond to inert HMX. For a tightly packed random grain distribution (with initial porosity of 19%) we varied the piston velocity to obtain weak partly compacted waves and stronger fully compacted waves. The average stress and wave speed are compatible with the porous Hugoniot locus for uniaxial strain. However, the heterogeneities give rise to stress concentrations, which lead to localized plastic flow. For weak waves, plastic deformation is the dominant dissipative mechanism and leads to dispersed waves that spread out in time. In addition to dispersion, the granular heterogeneities give rise to subgrain spatial variation in the thermodynamic variables. The peaks in the temperature fluctuations, known as hot spots, are in the range such that they are the critical factor for initiation sensitivity.

1 Introduction

It has long been known that hot spots, localized spatial peaks in the temperature field, play a dominant role in the initiation of heterogeneous explosives [1]. Numerical simulations of shock initiation by Mader [2, Sec. 3.3] show that hot spots generated by void collapse and impedance mismatches with impurities are critical factors in determining initiation sensitivity. In addition, weak shocks can desensitize an explosive by closing voids and thus decreasing the heterogeneities and eliminating sources of hot spots; see for example [3, 4] and [2, pp. 178–183].

Despite the importance of hot spots, current burn models are based on only bulk or spatially averaged thermodynamic variables. Models motivated by hot spots, such as the growth and ignition model [5] or the JTF model [6], are largely heuristic in nature. In effect, they use a sequence of reactions to simulate the effect of hot spots. The mass fraction of the reactant associated with hot spots is an input parameter and not a dynamic variable. This limits their domain of applicability. Bulk burn models can be effective for simulating the class of experiments in which the hot-spot distribution is close to the distribution of the experiment used to calibrate the model. Appropriately calibrated, bulk burn models have been successful at reproducing reaction wave profiles in shock-to-detonation transitions and in propagating detonation waves.

For weak stimuli, such as a low velocity impact that initiates a deflagration-to-detonation transition (DDT), predictions based on bulk burn models are qualitatively correct but quantitatively accurate in only a very limited regime. A predictive burn model over a wide range of conditions requires a more accurate description of the underlying physics. This strongly suggests introducing additional variables to characterize the hot-spot distribution and governing equations for their dynamical evolution. The stumbling block in developing such an improved burn model has been the lack of data. The spatial and temporal scales for hot spots is set by the grain size, and typically these scales are well below the experimental resolution of currently available diagnostic techniques. However, it is possible to do numerical experiments of small regions with high resolution. These computations, called micro-mechanical simulations, apply continuum mechanics to the meso-scale over which heterogeneities and hot spots occur and are expected to be statistically meaningful.

Just as physical measurements have experimental errors, numerical ex-

periments have uncertainties associated with the assumed constitutive properties of the material. Of particular importance for studying hot spots are the dissipative mechanisms in the model. For prompt shock initiation, the dominant heating mechanism is from void collapse. Material strength is negligible and a hydrodynamic model, as used in the simulation by Mader [2], suffices. At low pressures, comparable to the yield strength, other dissipative mechanisms are possible [7], such as plastic work, viscous heating in shear bands, and frictional heating at grain boundaries or along closed cracks. The dominant dissipative mechanism is likely to be application dependent.

Here we focus on compaction waves in granular explosives. This is of interest for several reasons. Granular explosives are used as a model for damaged explosives. Compared to solid explosives, the additional degree of freedom from porosity leads to an increased sensitivity to initiation. Porosity under compressive stress requires material strength. Even for weak waves, stress concentrations at the contact between grains leads to localized plastic deformation and heating, which gives rise to hot spots. The enhanced sensitivity of granular explosives to weak compaction waves is observed in DDT tube experiments; see for example [8]. In addition, compaction wave profiles from gas gun experiments [9] show evidence of burning.

In order to understand the structure of piston driven compaction waves in a granular material we have performed micro-mechanical simulations with the COMADREJA code. This is a two-dimensional Eulerian code developed by David Benson at the University of California, San Diego. A similar code called RAVEN has been used previously to study sintering or dynamic compaction of powdered metals [10, 11]. The 2-D calculations we present assume planar strain.

We use material properties and grain distribution corresponding to coarse HMX. With a porosity of about 20%, the grains in 2-D are mostly in contact, roughly speaking, a tightly packed random distribution. The piston velocity is varied from 200 m/s to 1000 m/s. The waves generated are nominally planar and range from weak partly compacted waves to strong fully compacted waves. We find that the mechanical wave properties, average pressure and wave velocity, closely correspond to the values on the porous Hugoniot locus for uniaxial strain. For weak waves, plastic deformation is the dominant dissipative mechanism and leads to dispersed waves that spread out in time. In addition to dispersion, the granular heterogeneities give rise to subgrain spatial variation in the thermodynamic variables. The temperature peaks or hot spots are in the range that would affect ignition.

Fluctuations are more sensitive than average quantities. They are affected by mesh resolution, the numerical treatment of grain interfaces, and the dissipative mechanisms giving rise to the wave profile. In addition, the pressure behind the compaction waves is well below the bulk modulus. Consequently, the equation of state (EOS) is stiff, and the stress is more sensitive to small variations in density than to variations in temperature. We believe the computed trends in the temperature variations are plausible, but there are uncertainties related to the simplified constitutive model and limitations in mesh resolution.

The following is an outline of the paper. The constitutive model used to characterize the HMX is specified in Section 2. This consists of a hydrostatic pressure and a simple elastic-plastic model for the shear stress. For comparison purposes the uniaxial strain Hugoniot for HMX is given in Section 3. The elastic-plastic transition is accounted for in the Hugoniot locus. In Section 4 the setup for the computations is discussed. Numerical results for compaction waves are presented and analyzed in Section 5. In Section 6 we discuss the extent to which homogenized continuum models capture the structure of the micro-mechanical based compaction wave profiles. A summary and conclusions on the effect of the granular heterogeneities on compaction waves are given in Section 7.

2 Constitutive Model

The material properties of HMX, for the purpose of this study, are described by a hydrostatic equation of state and a simple strength model for the stress deviator.

2.1 Hydrostatic Equation of State

A Mie-Grüneisen EOS is used for the hydrodynamic component of the constitutive model. It is based on the principal Hugoniot with a linear u_s - u_p relation and a Grüneisen coefficient of the form $\Gamma/V = \text{constant}$, see Appendix I. Parameters for the EOS are listed in Table 1 below. In the range of interest, up to ~ 10 GPa, this is nearly the same as the Hayes EOS calibrated for HMX in Ref. [12].

| | | | |
|------------|----------------------|-------------------|---------------------------------|
| c_0 | 2.65 | km/s | Bulk sound speed |
| s | 2.38 | — | Slope of u_s - u_p relation |
| Γ/V | 2.09 | g/cm ³ | Grüneisen coefficient |
| ρ_0 | 1.9 | g/cm ³ | Initial density |
| C_v | 1.0×10^{-3} | (MJ/kg)/K | Specific heat |

Table 1: Parameters for hydrostatic equation of state.

2.2 Strength Model

For simplicity the strength model assumes the material is isotropic. The stress deviator is based on a constant shear modulus and a perfectly plastic, rate-independent von Mises yield condition. See Appendix II. Parameters for the strength model are listed in Table 2 below.

| | | | |
|-----|------|-----|----------------|
| G | 10. | GPa | Shear modulus |
| Y | 0.37 | GPa | Yield strength |

Table 2: Parameters for strength model.

2.3 HMX Parameters

The key material parameters for HMX are listed in Table 3 below. The shear strain energy is not included in the EOS. The maximum shear energy is equivalent to a temperature rise of only $e/C_v = 1.2$ K, and to a thermal pressure of only $\frac{\Gamma}{V}e = 2.5 \times 10^{-3}$ GPa. Thus, the effect of elastic shear strain energy is negligible.

2.4 Additional Material Properties

HMX melts below the ignition temperature. At atmospheric pressure the melting temperature is $T_m^0 = 520$ K. The melting temperature increases with pressure. The temperature increase can be estimated based on the Kraut-Kennedy relation. See [13, Sec. 5.3.2].

$$T_m = T_m^0 \left(1 + C \frac{\Delta V}{V_0} \right) \quad (1)$$

| Moduli | | | |
|---------------|----------------------|-------|-----------------------------|
| K | 13.4 | GPa | Bulk modulus |
| G | 10. | GPa | Shear modulus |
| E | 24. | GPa | Youngs modulus |
| ν | 0.2 | — | Poisson ratio |
| sound speed | | | |
| c_l | 3.75 | km/s | Longitudinal sound speed |
| c_0 | 2.65 | km/s | Bulk sound speed |
| c_s | 2.30 | km/s | Shear sound speed |
| Elastic limit | | | |
| ϵ | 0.018 | — | Strain |
| u_p | 0.07 | km/s | Particle velocity |
| U_{el} | 3.9 | km/s | Wave speed |
| σ_{xx} | 0.52 | GPa | Stress |
| Y | 0.37 | GPa | Yield strength |
| e | 1.2×10^{-3} | MJ/kg | Maximum shear strain energy |

Table 3: Material parameters for HMX.

with $C = 2(\Gamma_0 - \frac{1}{3})$. For the strongest compaction waves we consider, pressure ≈ 50 kb, $\frac{\Delta V}{V_0} \approx 0.1$, and the melting temperature increases to about 600 K. The effect of the latent heat, $Q_m = 0.22$ MJ/kg, corresponds to a temperature of $\Delta T = Q_m/C_v = 220$ K, and a thermal pressure of $\frac{P}{V} Q_m = 0.46$ GPa. Since the reaction rate is sensitive to temperature, latent heat has an important effect on ignition due to weak stimuli such as compaction waves. The hydrostatic model in the code accounts for the effects of latent heat on the temperature and on the thermal component of the pressure. It is not refined enough to account for the small volume change when the material melts.

Upon melting the yield strength and shear modulus vanish. As a result melting limits the plastic work to be less than $C_v(T_m - T_0) = 0.25$ MJ/kg, where the initial temperature is $T_0 = 300$ K. We note that the plastic work is comparable to the latent heat of melting. The limit on the plastic work places a bound on the plastic strain, $\epsilon_p < C_v(T_m - T_0)/Y = 0.7$. In addition, above melting the shear viscosity decreases and lowers the shear heating. Only our later simulations have accounted for the change in yield strength and shear modulus on melting. The effect of melting on the tail of the temperature

distribution will be discussed in more detail later.

The constitutive model neglects several other material properties. In particular, the grains are small crystals of β -phase HMX. The crystal structure is monoclinic. The individual components of the elastic tensor have not yet been determined. Single crystal wave profiles measured by Jerry Dick *et al.* [14, Fig. 34] show an orientation dependence. In addition, the profiles show that the plastic wave has a rise time of 50 to 100 ns. Thus, plasticity is rate dependent. For simplicity the anisotropy and rate dependence of the plasticity are neglected. Also, the wave profiles imply the yield strength is closer to 0.3 GPa, which is 20% smaller than the value in Table 2. In addition, just before melting HMX undergoes a polymorphic phase transition from the β -phase to the δ -phase. This effect is neglected.

Quasi-static compaction experiments indicate that the grains are brittle and fracture [15, 16]. The constitutive model neglects fracture. Also neglected is friction as the grains slide over one another. However, the simulations used a shear viscosity with a coefficient of 310 Poise ($0.031 \text{ GPa} \cdot \mu\text{s}$) below melting and 0.14 Poise above melting.¹ In addition to plastic work and viscous shear work, the calculations have a flux-limited artificial bulk viscosity (Christensen’s modification to the von Neumann-Richtmeyer form; see ref. [17]) for the dissipation mechanisms.

Finally, the material is assumed to be inert. The simulations discussed here are aimed at understanding the mechanical properties of compaction waves and the fluctuations that can be expected from the granular heterogeneity. Later we plan on studying the burn rate due to the hot spots.

3 Hugoniot Locus

The 1-D Hugoniot locus for uniaxial strain provides a point of comparison that is helpful in understanding the effects of heterogeneities on compaction waves in granular materials. To account for the porosity, the fluid equations must be supplemented with the additional variable for the solid volume fraction ϕ . The simplest description of a granular material is given by the Herrmann-Carrol-Holt P - α model [18, 19]. (Note, the distension $\alpha = 1/\phi$.) This consists of the conservation equation for fluid flow of an elastic-plastic

¹Values for shear viscosity suggested by Paul Conley, Univ. of Calif. San Diego.

material

$$\frac{\partial}{\partial t} \begin{pmatrix} \rho \\ \rho u \\ \rho E \end{pmatrix} + \frac{\partial}{\partial x} \begin{pmatrix} \rho u \\ \rho u^2 + \sigma_{xx} \\ \rho u(E + \sigma_{xx} V) \end{pmatrix} = \vec{0}, \quad (2)$$

where the total specific energy is $E = e + \frac{1}{2}u^2$, together with a constitutive relation defining the component of the stress in the direction of wave propagation σ_{xx} and a relation for the equilibrium volume fraction ϕ .

The P - α model relates the average material pressure to the pressure of the pure solid and the porosity. In the same spirit, we relate the average material stress to the stress in the pure solid. This modification enables the porous Hugoniot locus to converge to the solid Hugoniot locus in the limit as the porosity goes to zero. In the simplified model the porous stress is assumed to be

$$\sigma_{xx} = \phi \cdot [P_s(V_s, e) + \frac{4}{3}G \epsilon_{el}], \quad (3)$$

where the specific volume of the pure solid is $V_s = \phi/\rho$, the elastic strain is

$$\epsilon_{el} = \min\left(\ln(V_{s0}/V_s), \epsilon_Y\right), \quad (4)$$

and $\epsilon_Y = \frac{Y}{2G}$ is the strain on the yield surface. For simplicity, we assume that the equilibrium volume fraction is given by

$$\phi = 1 - (1 - \phi_0) \exp(-P_s/P_c), \quad (5)$$

where P_c is a characteristic pressure. The characteristic pressure is related to the yield strength. A value of $P_c = 0.1$ GPa gives about the right crush-up pressure for HMX. Better fits to the equilibrium volume fraction can be based on data from quasi-static compression experiments [15].

Steady state waves are determined by the Hugoniot equation

$$e - e_0 = 0.5 [\sigma_{xx} + (\sigma_{xx})_0] \cdot (V_0 - V) \quad (6)$$

together with the constitutive relations Eqs. (3)–(5). The Hugoniot loci for the pure solid and a porous solid with $\phi = 0.81$ are shown in Fig. 1. For the pure solid, we note that plastic yield gives rise to a two-wave structure (elastic precursor followed by plastic wave) for piston velocities from 70 to 400 m/s.

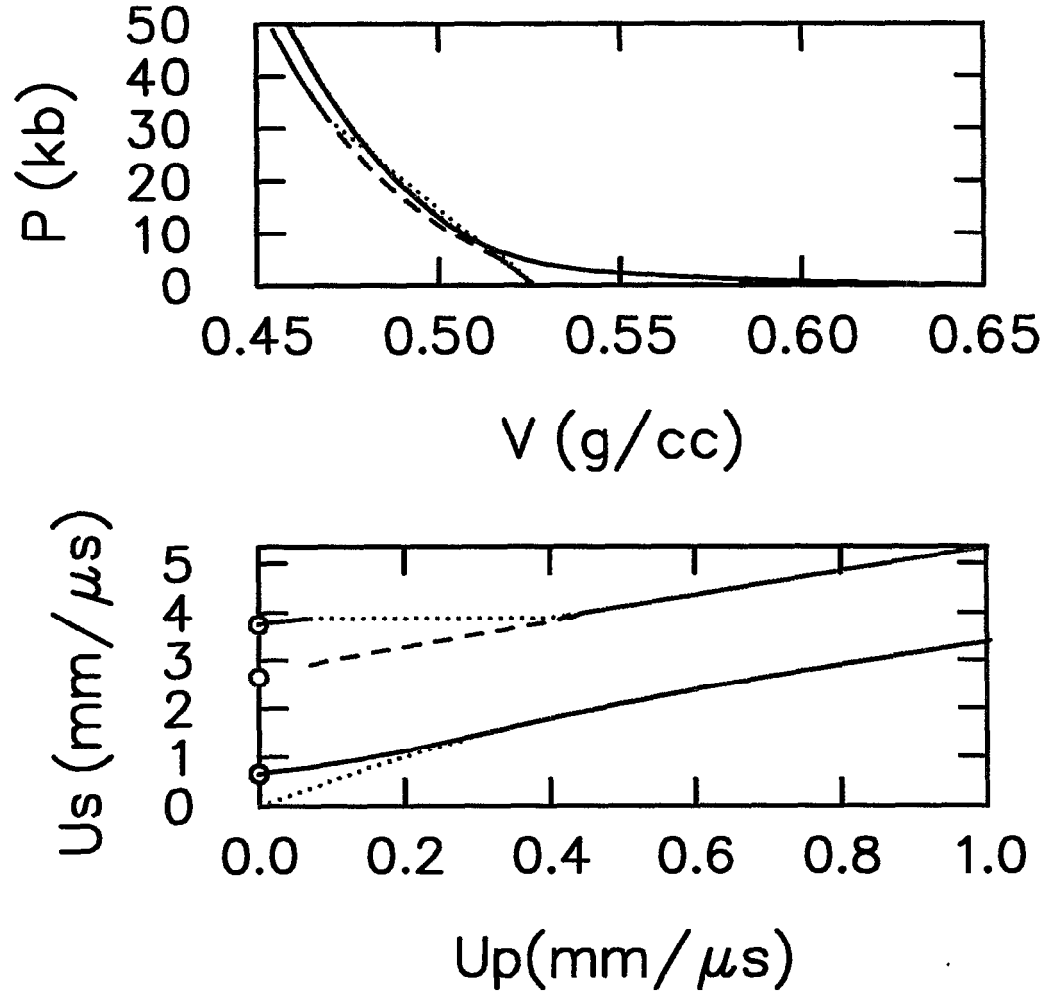


Figure 1: Hugoniot loci. Solid black line is porous Hugoniot ($\phi = 0.81$). Dotted red line is fully compacted Hugoniot ($\phi = 1$). Blue lines are pure solid Hugoniot; dashed line corresponds to plastic wave following elastic precursor, and dotted line corresponds to Rayleigh line for elastic precursor in the range of the two-wave structure.

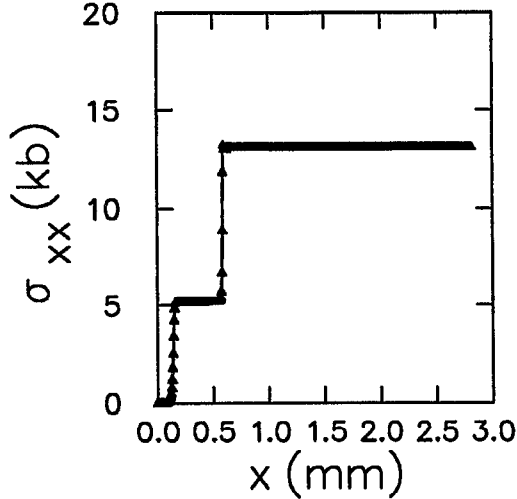


Figure 2: Stress profile for piston velocity of 200 m/s at $t = 0.7 \mu\text{s}$. Symbols indicate value at center of cells.

In this simple 1-D model, porosity leads to a lower sound speed and eliminates the two-wave structure due to the elastic-plastic transition.

A numerical example of the two-wave structure is shown in Fig. 2. Since the plastic strain is determined by rate independent plasticity, the plastic wave corresponds to a shock. The artificial viscosity is chosen just large enough such that the plastic wave profile is spread out over enough cells to avoid oscillations in the plastic strain and hence in the stress. The same viscosity coefficients are used for the 2-D simulations.

The temperature on the Hugoniot loci is shown in Fig. 3. For a given pressure, the temperature on the porous Hugoniot locus is significantly larger than on the pure solid Hugoniot locus because of the increased ΔV due to the change in volume fraction. The induction time as a function of hot spot radius and temperature can be computed based on an Arrhenius reaction rate [20]. With the parameters for HMX given in Table 4 the induction times are shown in Fig. 4. If ignition depended on the thermal properties of only the bulk material, then the two figures combined would imply that a 70 kb shock in the granular HMX (19% porosity) would be needed to achieve a bulk temperature of 650 K sufficient for prompt ignition (induction time of less than $1 \mu\text{s}$) and that a much stronger shock would be needed for solid HMX. We note that the granular material melts below the ignition temperature.

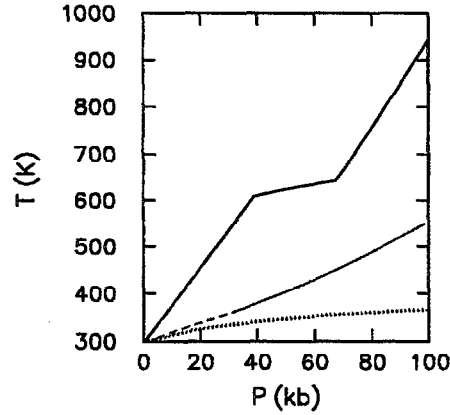


Figure 3: Hugoniot loci and isentrope. Solid black line is porous Hugoniot ($\phi = 0.81$); change in slope around 650 K is due to melting. Blue lines are pure solid Hugoniot. Blue and black dotted lines are temperature on isentrope to same specific volume as on corresponding Hugoniot loci.

| | | | |
|----------------------------------|----------------------|---|------------------------|
| Z | $5. \times 10^{13}$ | μs^{-1} | Pre-exponential factor |
| T_a | 2.5×10^4 | K | Activation temperature |
| Q | 5. | MJ/kg | Heat release |
| κ | $4. \times 10^{-10}$ | $\text{kJ}/(\text{m} \cdot \mu s \cdot \text{K})$ | Thermal conductivity |
| C_p | 1.5×10^{-3} | $(\text{MJ}/\text{kg})/\text{K}$ | Specific heat |
| $\chi = \frac{\kappa}{\rho C_p}$ | 1.4×10^{-7} | $(\text{mm})^2/\mu s$ | Thermal diffusivity |

Table 4: Parameters for HMX hot spots.

For the same temperature the solid would not have melted since its Hugoniot pressure is higher leading to a higher melt temperature. The rate constants for solid HMX are slower than those of liquid HMX, see [2, p. 218] and [4].

It is important to note that a 3 kb shock in granular HMX raises the bulk temperature by only 22 K. Despite this small temperature rise a delayed detonation occurs in DDT tube experiments [8]. In contrast, negligible reaction results from quasi-static compression to the same pressure. The micro-mechanical simulations described below are aimed at determining the hot-spot distribution resulting from compaction waves in a granular bed. For weak waves, plastic work from grain distortion is expected to be a significant dissipative mechanism.

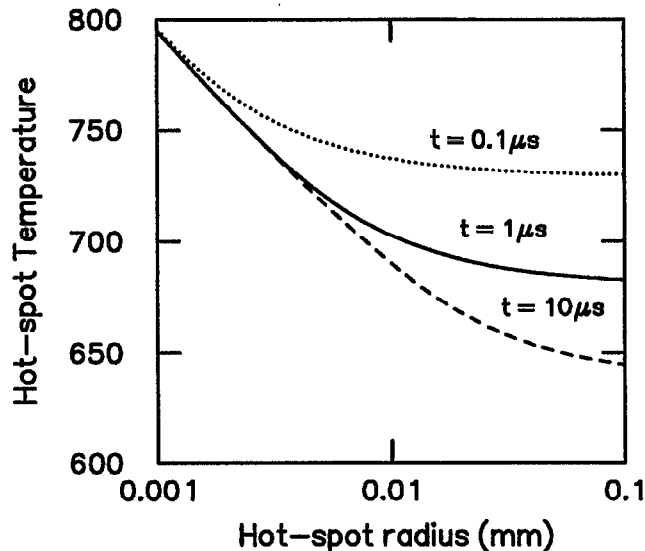


Figure 4: Contours of induction time as function of hot spot radius and hot spot temperature (for ambient temperature of 300 K).

4 Numerical Model

For our simulations of compaction waves the granular bed consists of a rectangular region. The waves are driven by a planar piston moving from right to left. Thus, the x-axis is the direction of wave propagation, and the y-axis is parallel to the wave front.

The natural length scale for the bed is the grain size. Even though the wave is nominally one-dimensional, to adequately describe the two dimensional effects from the heterogeneities a minimum of about 10 grains are needed for the bed width. Periodic top and bottom boundary conditions are used to minimize effects from the boundaries parallel to the wave propagation direction. A bed length of about 30 grains is used in order to give start-up transients a chance to die down and achieve on average a steady wave profile. Thus, the granular bed has an aspect ratio of about 3 to 1.

The overall size of the granular bed, roughly 30 grains by 10 grains, and the available computing power then determines the resolution. The workstation we are using for the calculations (SUN SPARC Ultra I, 140 Mhz,

which has about the same power as a 200 Mhz Pentium Pro PC) allows a resolution of about 15 cells per grain diameter on a uniform mesh. Each simulation takes between a couple of days and a week.

4.1 Granular Distribution

The granular bed is chosen to have tightly packed, randomly distributed grains. The grain packing algorithm has two stages. In the first stage an initial packing is generated in which grains are allowed to overlap. The second stage is based on a “molecular dynamics” approach where forces and torques arising from overlaps are used to adjust the grain positions in order to eliminate overlaps. The number and size distribution of grains is fixed at the beginning of the process, and the size of the box is determined by the desired porosity. The starting configuration is generated by randomly placing the grains, in order of decreasing size, in the box. The only constraint applied is that the position of the center of a newly introduced grain not be within the occupied volume of existing grains. This corresponds roughly to having less than 50% initial overlap between pairs of grains. The forces and torques between grains are assumed to be proportional to the amount of overlap (volume or area) between neighboring grains. The resulting grain displacement is calculated to diminish the sum of forces on each grain. The grains are assumed to be rigid and their mass proportional to their size. Damping is applied by restricting the displacement to $\sim 10\%$ of the diameter of the grain. For the second stage, either the absolute linear dimensions of the box or the aspect ratio of the linear dimensions of the box can be specified provided that the total volume is preserved. Either fixed or periodic boundary conditions can be applied. For circular grains a solid volume fraction of 0.81 or a porosity of 19% is readily obtained. For comparison, a regular array of closed packed circles has a porosity of $1 - \frac{\pi}{2\sqrt{3}} = 9.3\%$.

Calculations were done with two grain size distributions. Initially a log-normal size distribution, shown in Fig. 5, was chosen to match coarse grain HMX. Because the resolution requirement from the small grains limited the length of the bed, most of our simulations used an approximate mono-dispersed size distribution. The “mono-dispersed” distribution had a mean grain diameter of $140\text{ }\mu\text{m}$ with a uniform variation of $\pm 10\%$. For this distribution, a cell size of $10\text{ }\mu\text{m}$ is used. The overall computational mesh consisted of 518×150 cells or $5.18\text{ mm} \times 1.5\text{ mm}$. The length is comparable to the granular sample (3.9 mm) used in the gas gun experiments [9].

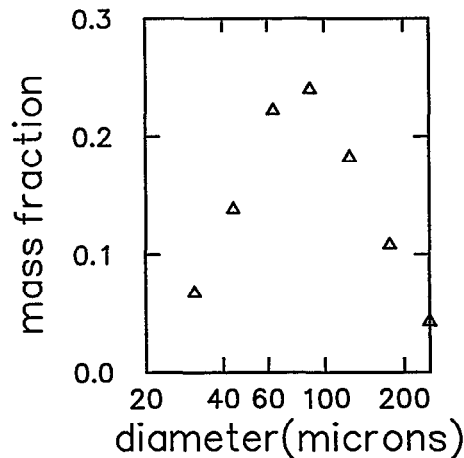


Figure 5: Grain distribution for coarse HMX.

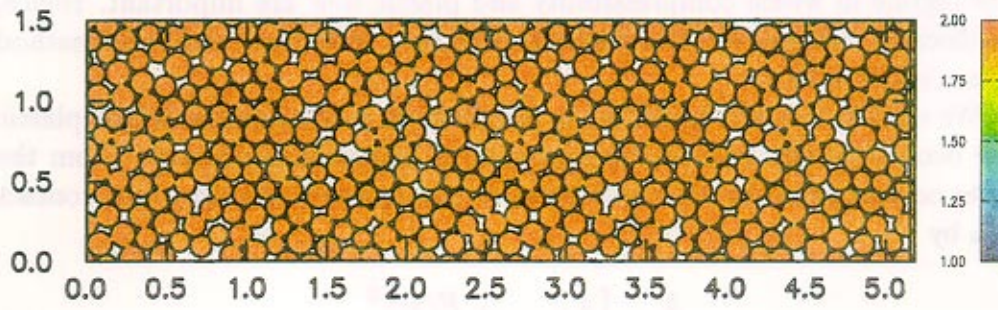
The mono-dispersed granular bed is shown in Fig. 6. It contains a total of 432 grains (shown in red). The porosity profile shows that there are short wavelength fluctuations with a large amplitude. The average porosity is 0.19, and the standard deviation is 0.05. Averaging over 2 grain diameters (0.28 mm) greatly reduces the peak fluctuations. The averaged porosity is then $19 \pm 3\%$, and the variations have a wavelength of ~ 1 mm. The fluctuations in porosity result in a $\pm 4\%$ variation in the average density. Based on the Hugoniot relations for a homogenized continuum model, the relatively long wavelength density variation will contribute to fluctuations behind a compaction wave.

4.2 Dimensionality and Smallest Length Scale

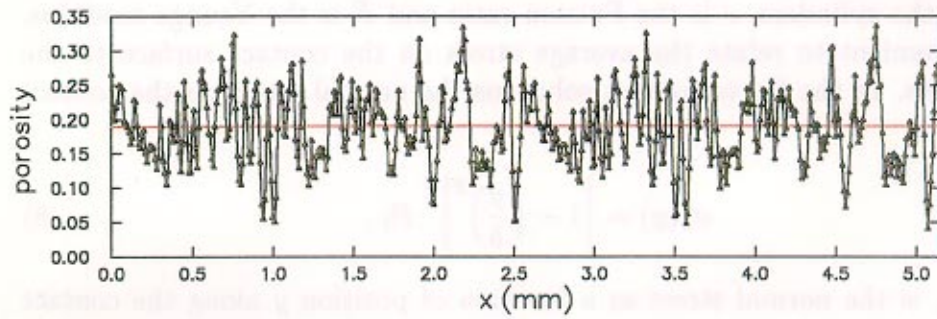
When two grains are pressed together, they distort elastically. The area of the contact surface at which plastic flow first occurs sets a length scale for assessing how well a micro-mechanics calculation of granular flow is resolved. For a linearly elastic material and circular or spherical grains, the static stress and strain fields are given analytically by the Hertz contact solution; see for example, [21] or [22].

We note in passing that contact forces are the basis for the discrete element method first introduced for applications in soil mechanics [23]. These methods have evolved and have recently been used to study shear flows in

a) Density



b) Porosity profile



c) Porosity, smoothed with running average over 2 grain diameters

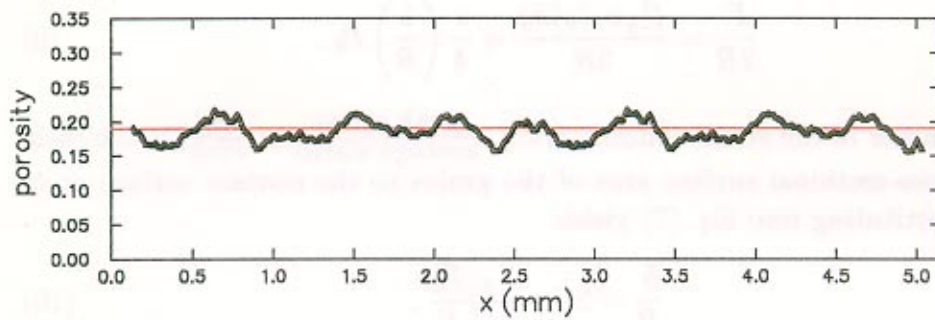


Figure 6: Mono-dispersed granular bed. Initial porosity is 19%.

granular materials [24]. They are suited to the low pressure regime in which compressibility can be neglected. Compaction waves involve a higher pressure regime in which compressibility and plastic flow are important. Hence, the discrete methods are complementary to the continuum mechanics method we are employing.

We outline the derivation of the elastic limit or the point at which plastic flow occurs for the two-dimensional case of cylinders in contact. From the Hertz contact solution, the force between two grains is related to the contact area by

$$\frac{b}{R} = \left[\frac{4}{\pi} (1 - \nu^2) \frac{F/R}{E} \right]^{\frac{1}{2}}, \quad (7)$$

where R is the radius of the cylinder, $2b$ is the length of the contact surface in the plane normal to the cylindrical axis, F is the force per unit length between the cylinders, ν is the Poisson ratio and E is the Young's modulus. It is convenient to relate the average stress on the contact surface to the peak stress. In the Hertz contact solutions the normal stress on the contact surface is

$$\sigma_z(y) = \left[1 - \left(\frac{y}{b} \right)^2 \right]^{\frac{1}{2}} P_0, \quad (8)$$

where σ_z is the normal stress as a function of position y along the contact surface ($-b \leq y \leq b$) and P_0 is the peak stress which occurs at the center of the contact surface. From this we obtain the average stress (for cross section of the grain)

$$\frac{F}{2R} = \frac{\int_{-b}^b \sigma_z(y) dy}{2R} = \frac{\pi}{4} \left(\frac{b}{R} \right) P_0. \quad (9)$$

A large factor in the stress concentration, $\frac{\text{peak stress}}{\text{average stress}} = \frac{P_0}{F/2R}$, is the ratio of the cross-sectional surface area of the grains to the contact surface area, R/b . Substituting into Eq. (7) yields

$$\frac{b}{R} = 2(1 - \nu^2) \frac{P_0}{E}. \quad (10)$$

The maximum principle shear stress [21, Eq. (42.16)] occurs a distance $z/b = 0.768$ from the center of the contact surface in the normal direction

and has a value $\tau_{\max} = 0.3P_0$. With the von Mises criterion, yield first occurs when

$$Y = \sqrt{\frac{3}{2}} \|\boldsymbol{\sigma}'\| = \sqrt{3} \tau_{\max} = 0.3\sqrt{3} P_0 , \quad (11)$$

where Y is the yield strength. It then follows that plastic flow begins when

$$\frac{b}{R} = \frac{2}{0.3\sqrt{3}}(1 - \nu^2)\frac{Y}{E} . \quad (12)$$

The analogous results for the three-dimensional case of the contact between spheres are given as follows. The average stress in terms of the peak stress is

$$\frac{F}{(2R)^2} = \frac{\pi}{6} \left(\frac{b}{R}\right)^2 P_0 , \quad (13)$$

where now F is the force and b is the radius of a circular contact surface. We note that the stress concentration factor is larger for spherical grains than for circular grains since in 3-D it is proportional to $(R/b)^2$ while in 2-D it is linear in R/b . Yield occurs when

$$Y = \sqrt{\frac{3}{2}} \|\boldsymbol{\sigma}'\| = 2\tau_{\max} \approx \frac{2}{3} P_0 , \quad (14)$$

The contact surface radius at yield is given by

$$\frac{b}{R} = 3\pi(1 - \nu^2)\frac{Y}{E} . \quad (15)$$

In 3-D the average stress at yield is proportional to $(Y/E)^2Y$ while in 2-D it is proportional to $(Y/E)Y$. Since Y/E can be on the order of 0.01, the average stress can be much smaller for spherical grains than for circular grains. This is one important difference due to dimensionality between 2-D calculations and physical 3-D grains.

The values of important parameters characterizing the elastic limit of the Hertz contact solution for HMX are listed below in Table 5.

The Hertz solution is based on the assumption that the change in grain radius is small. The change in radius is given by

$$\frac{\Delta R}{R} = 1 - \left[1 - \left(\frac{b}{R}\right)^2\right]^{\frac{1}{2}} \approx \frac{1}{2} \left(\frac{b}{R}\right)^2 . \quad (16)$$

| | 2-D | 3-D | | |
|----------------|------|------|------|-----------------------------|
| b/R | 5.5 | 3.6 | % | Linear contact length |
| $\Delta R/R$ | 0.15 | 0.07 | % | Fractional change in radius |
| P_0 | 0.64 | 0.56 | GPa | Peak stress |
| average stress | 280 | 3.8 | bars | Average stress |

Table 5: Elastic limit of Hertz contact solution for HMX.

From the table, up to the elastic limit the Hertz solution is valid.

For our calculations, which have a resolution of only 14 cells per grain diameter, the contact surface at yield is less than 1 cell. This affects weak compaction waves (stress of less than say 0.5 kb) for which elasticity dominates the stress. In particular, the plastic dissipation when the change in porosity is small is not accurately calculated. This also affects the weak elastic precursor to stronger compaction waves.

Another difference between 2-D calculations and physical 3-D granular beds is related to the porosity and number of contacts per grain. For example, we can compare dense packed regular arrays in 2-D and 3-D. Circular grains in 2-D have a maximum porosity of $1 - \frac{\pi}{2\sqrt{3}} = 9.3\%$ and 6 contacts per grain, while spherical grains in 3-D have a maximum porosity of $1 - \frac{\pi}{3\sqrt{2}} = 26\%$ and 12 contacts per grain. For random packing analytic formulae are not available. The dimensionality of packing leads to difficulties in generating granular beds for 2-D computations with the same porosity as used in experiments, especially for high porosity loose packings. Even with the same porosity, there are uncertainties in comparing numerical wave profiles calculated in 2-D with experimentally measured wave profiles that are inherently 3-D. Moreover, the hot-spot distribution can be expected to depend on the number of contacts per grain and hence vary with dimensionality.

4.3 Algorithmic Considerations

Since we are interested in hot spots, it is natural to consider the effect of heat conduction. The scale over which heat conduction has an effect is on the order of $\Delta x = [\chi \Delta t]^{\frac{1}{2}}$. The value of the thermal diffusivity for HMX from table 4 is $\chi = 1.4 \times 10^{-7} (\text{mm})^2/\mu\text{s}$. The time covered by our compaction wave simulations is about $1 \mu\text{s}$. Over this time period, heat conduction can smooth out temperature variations over a length of only $\frac{1}{3} \mu\text{m}$. This length is

30 times smaller than the cell size. Hence, heat conduction is not significant at the resolution in our simulations.

Large distortions of the grains are required to fully compact the bed. Most of the shear strain is plastic since the yield strength limits the magnitude of the elastic strain to a small value (from Table 3, $\epsilon_{el} \leq 0.018$). Even though the plastic strain is large, the model we are using for the shear stress is a reasonable approximation when the elastic strain is small.

The finite difference algorithm we are using is second order accurate in smooth regions. However, most of the dissipative effects that give rise to hot spots occur at or near grain boundaries. The algorithm treats the boundary between a grain and a pore (void) as a material interface. In addition, even though all the grains have the same constitutive properties, to track grain distortion individual grains are considered to be different materials. Consequently, the boundary between neighboring grains is also treated as a material interface. Interfaces have a lower accuracy than smooth regions. In an Eulerian algorithm, the interface between materials gives rise to mixed cells. The velocity within a cell is assumed to be constant. This implies a no-slip boundary condition at material interfaces.

Mixed cell algorithms are a continuing subject of research; see for example [25]. The mixed cell constitutive relation we are using assumes a uniform strain rate in each cell and then performs 1 step of a pressure equilibrium iteration. Thus, the materials within a mixed cell can be out of mechanical and thermal equilibrium. The advective stage of the algorithm uses the mixed cell partition of the component volumes and energies in conjunction with an interface reconstruction algorithm based on the material volume fractions of neighboring cells.

For the compaction waves we are simulating, the stress is well below the bulk modulus. Consequently, the material is stiff, and the stress is more sensitive to small changes in density than to the energetics. Since only 14 cells are used to resolve a grain, about half the mass of the grain is within two cells of the interface. As a result of the stiff equation of state and the limited resolution, the computed fluctuations in the temperature are expected to be less accurate than the average mechanical wave properties. For this reason we emphasize qualitative effects and trends with varying piston velocity.

5 Numerical Results

We compare compaction waves with three different piston velocities. The average effect of the heterogeneities can be judged by comparing with the predictions of the porous Hugoniot for uniaxial-strain listed in table 6 below. In addition, we describe the fluctuations resulting from the granular structure of the bed.

| | | | | | |
|---------------|------|------|------|------|-----------------------|
| u_p | 200 | 500 | 1000 | m/s | Piston velocity |
| u_s | 1100 | 2100 | 3400 | m/s | Wave speed |
| ϕ | 0.98 | 1 | 1 | – | Solid volume fraction |
| σ_{xx} | 3.4 | 16 | 52 | kbar | Stress |
| T | 322 | 424 | 720 | K | Temperature |

Table 6: State behind compaction based on porous Hugoniot for uniaxial-strain.

For pure HMX, the 200 m/s piston would give rise to a split wave structure (elastic precursor followed by plastic shock shown in Fig. 2), and the 1000 m/s piston is fast enough such that the plastic wave outruns the elastic precursor. The 500 m/s piston is an intermediate case. The porous Hugoniot predicts the wave is above the crush-up pressure and is fully compacted. In contrast the wave driven by the 200 m/s piston is only partly compacted. These three cases illustrate the qualitative changes in the wave profile as the wave strength increases.

5.1 Comparison with Piston Velocity

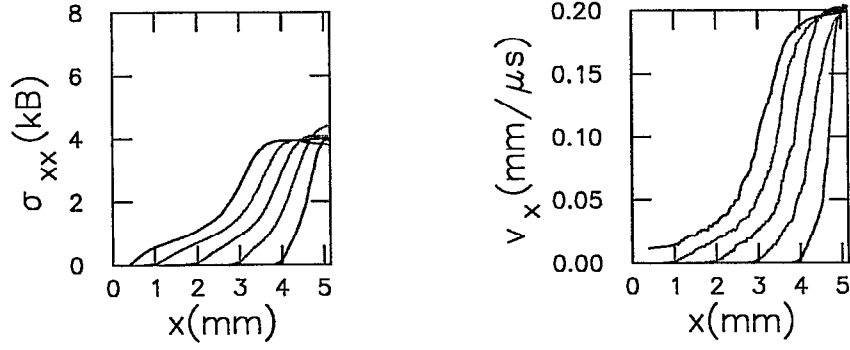
For all the simulations the piston is initially at the right boundary. At $t = 0$, it is impulsively started and moves to the left. Two types of plots are used to display the numerical results: 2-D plots in which the value of a variable is indicated by color, and 1-D plots of profiles. For the 2-D plots, voids and the region through which the piston has moved are indicated in gray. Superimposed in black are the interfaces of the grains obtained from contour levels of the material component volume fractions. These interfaces are displayed as a diagnostic to indicate the distortion of the grains and are not used by the code for evolving the flow. The x and y coordinates are in mm. The 1-D profiles are averages over the y-direction, *i.e.*, transverse to

the direction of wave propagation. A triangular symbol is plotted for each cell to indicate the resolution. In addition, the dashed lines represent the minimum and maximum values.

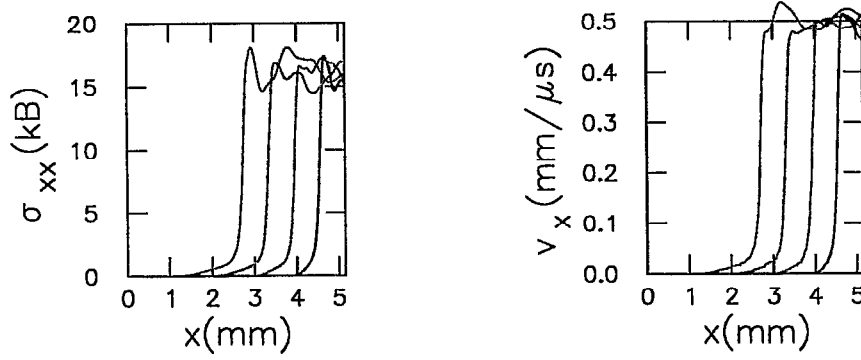
1. The time evolution of stress and velocity profiles are shown in Fig. 7. The profiles are relative to the piston whose position is translated to its initial value. These profiles are indicative of a propagating wave, though the material heterogeneities give rise to some fluctuations behind the wave front. The long wavelength fluctuations in the wave profile are due to the statistics of the grains, which, as discussed in Subsection 4.1, result in long wavelength variations in the initial density. The wave profiles are approximately steady at the end of the runs. We examine in detail the wave structure at the last time displayed.
2. The stress profiles and the stress fields (σ_{xx}) are shown in Figs. 8 and 9. The wave driven by the 200 m/s piston is only partly compacted, as shown by porosity profile in Fig. 10. The other two cases are fully compacted, *i.e.*, zero porosity behind the wave front. On the stress profiles, the predictions from the porous Hugoniot for uniaxial strain are superimposed in red; the horizontal line is the value of the stress, and the vertical line is the position of the shock. The stress is slightly low for the 200 m/s piston. This is due to the simple approximation for the equilibrium volume fraction used to calculate the Hugoniot locus. The approximation gives a volume fraction of 0.98 while the value in the simulation is about 0.95. Correcting for the volume fraction would raise the stress and the wave speed. As shown in green this is closer to the simulation. The other two cases are not sensitive to the chosen equilibrium volume fraction since their wave pressures are well above the crush-up pressure, and the waves are fully compacted, *i.e.*, $\phi = 1$. The shock being slightly behind the prediction is in part due to the time delay in forming the shock profile. For all three cases, the average numerical results are in good agreement with the Hugoniot.

The minimum and maximum values are also shown on profiles. This is an indication of the range of the spatial variation. The relative amplitude of the variation is quite large for the low piston velocity case. In addition, we note that portions of some grains go into tension. Very likely this is due to side rarefaction within a grain. Since HMX is

a) $u_p = 200$ m/s, profiles at $t = 0.4, 0.8, 1.2, 1.6, 2.0 \mu s$



b) $u_p = 500$ m/s, profiles at $t = 0.4, 0.8, 1.2, 1.6 \mu s$



b) $u_p = 1000$ m/s, profiles at $t = 0.2, 0.6, 1.0, 1.4 \mu s$

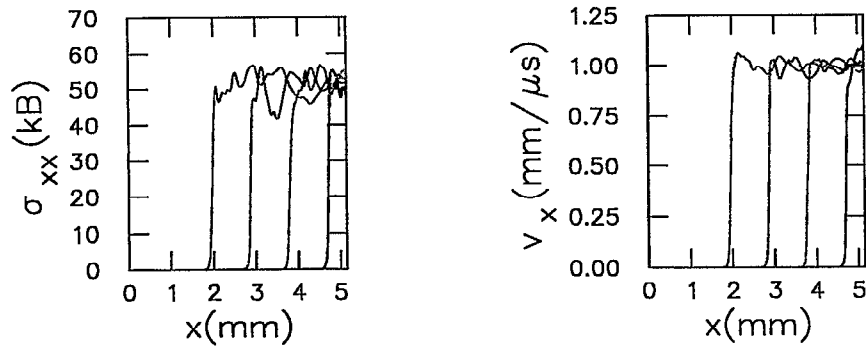
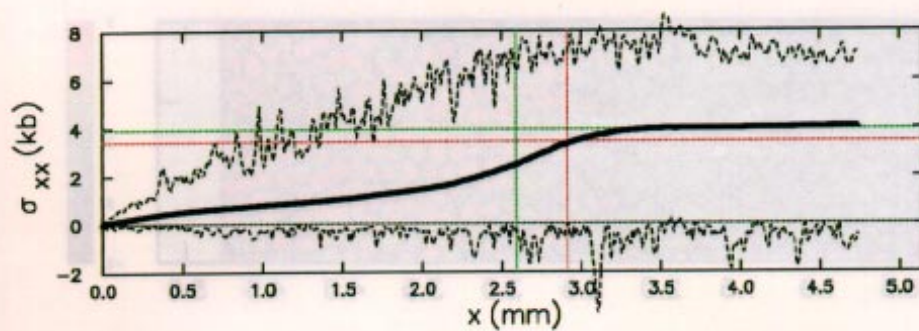
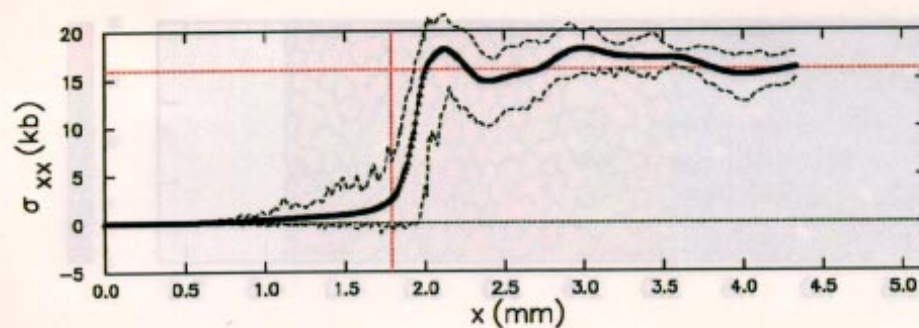


Figure 7: Time evolution of stress and velocity profiles.

a) $u_p = 200 \text{ m/s}$ at time = $2.0 \mu\text{s}$



b) $u_p = 500 \text{ m/s}$ at time = $1.6 \mu\text{s}$



c) $u_p = 1000 \text{ m/s}$ at time = $1.4 \mu\text{s}$

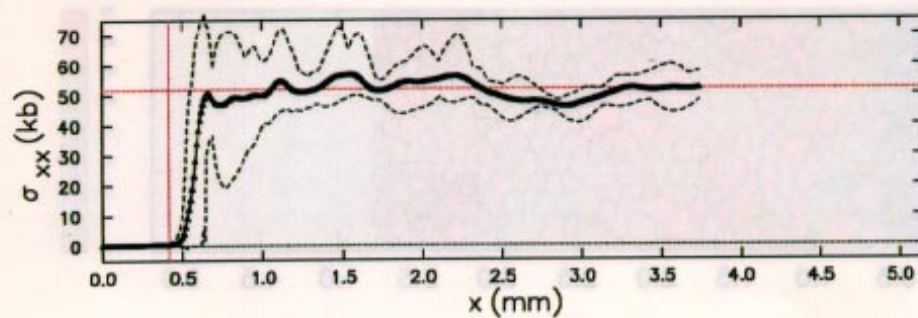
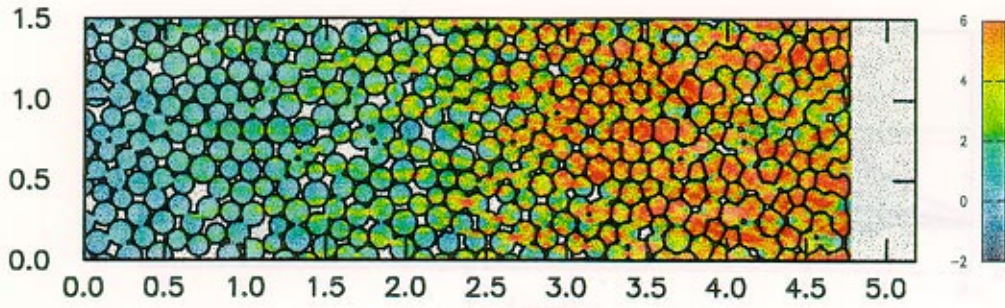
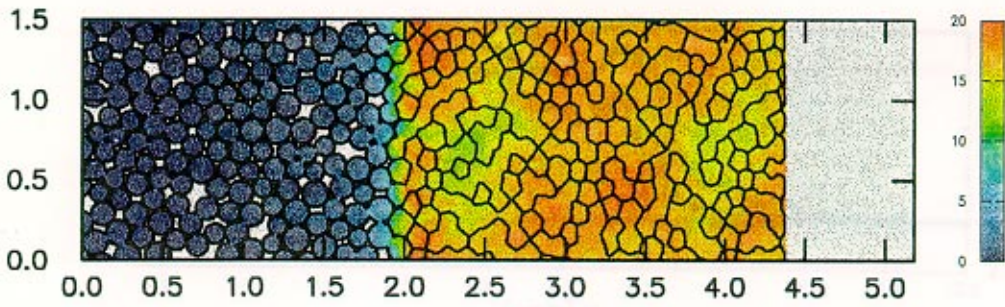


Figure 8: Stress profile (σ_{xx}) of compaction waves.

a) $u_p = 200$ m/s at time = $2.0 \mu\text{s}$



b) $u_p = 500$ m/s at time = $1.6 \mu\text{s}$



c) $u_p = 1000$ m/s at time = $1.4 \mu\text{s}$

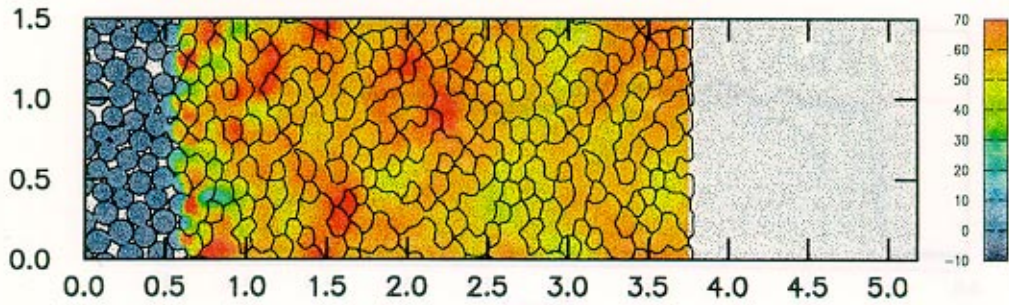


Figure 9: Stress field (σ_{xx}) of compaction waves. Pressure scale on color bar is in kb.

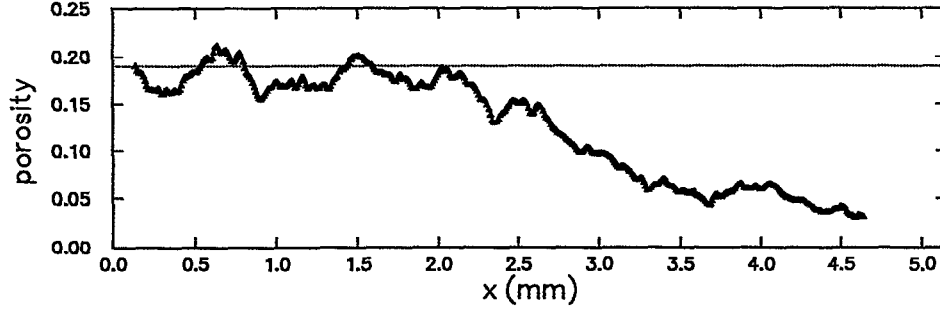


Figure 10: Porosity profile at $t = 2.0 \mu\text{s}$ of compaction wave driven by 200 m/s piston. Profile has been smoothed by taking running average over a length of 2 grain diameters. Dotted line is the average initial porosity (19%).

brittle, tension would cause them to fracture. Fracture is not included in the constitutive model used for the simulations.

There is a qualitative difference in the profiles for the three cases. For the 200 m/s piston, the wave profile is very spread out. The profile for the 500 m/s piston has a precursor and then a steep gradient. For the 1000 m/s piston the wave profile rises abruptly without a precursor. For a pure solid the precursor corresponds to the elastic wave in the 2-wave structure due to the elastic-plastic transition. In contrast to the pure solid, the porous material precursor is spread out and not like a shock. As with the pure solid, the precursor is not present when the plastic wave is strong enough to propagate faster than the elastic wave. Later we characterize the precursor in more detail.

The 2-D plot for the low velocity case shows that the stress behind the wave is very non-uniform due to stress fingering. This is the analog of stress bridging that has been studied for statically loaded granular beds; see for example, [26] and reference contained therein. The stress fingering occurs in the precursor region for both the 200 and 500 m/s piston. It is not as apparent in the plot for the 500 m/s piston because of the larger range of the stress scale. Stress fingering gives rise to larger stress concentrations than the estimate in Subsection 4.2 and leads to some plastic deformation even at very low average stresses. The resulting plastic dissipation affects the wave profile by damping

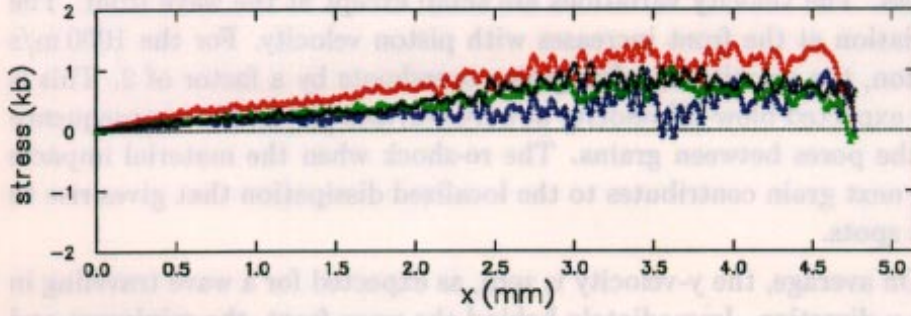
the precursor.

In contrast to the low piston velocity case, when the piston velocity is larger, the grains are severely distorted behind the wave front. Other researchers have referred to the low velocity cases as quasi-static compression and the high velocity cases as dynamic compression. See for example [11]. The plastic deformation in the high velocity cases is a major source of dissipation. The non-uniform manner in which the grains distort is a large source for temperature variations on a subgrain scale. Despite the non-uniformity of the granular bed, the wave front is fairly planar, and the wave width is on the order of 1 to 2 grain diameters.

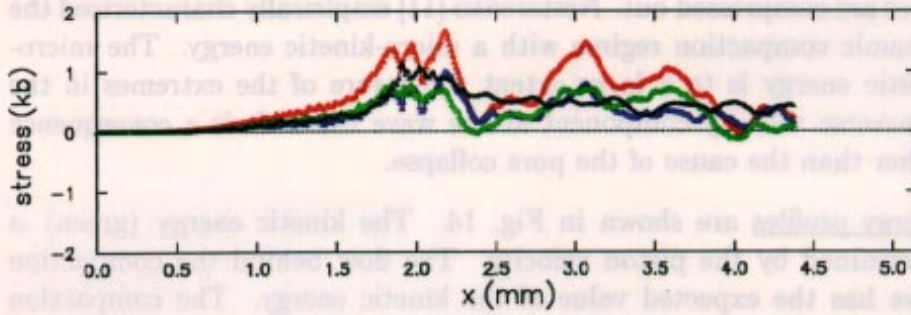
The Hugoniot locus only determines the component of stress in the direction of wave propagation. Though the computed stress σ_{xx} agrees well with the Hugoniot, the stress is a tensor. The components of the stress deviator are shown in Fig. 11. For the stronger fully compacted waves, the stress deviator appears to be relaxing towards 0. This is in contrast to a pure solid for which the stress deviator behind a plastic wave is $\sigma'_{xx} = \frac{2}{3}Y = 2.5 \text{ kb}$. Most likely the relaxation is due to acoustic waves behind the wave front generated by long wavelength stress fluctuations which arise from the local variations in the initial density due to the grain statistics. A visco-elastic continuum model [27, 28] has been used to describe this relaxation behavior in porous materials. For strong fully compacted waves, a hydrostatic equation of state is adequate to obtain the state behind the wave.

For the 200 m/s piston the wave is only partly compacted, and σ'_{xx} appears to be approaching about 1 kb. This is only 40% of the value for the homogeneous case. Consequently, our approximation for the stress, Eq. (3), used in computing the Hugoniot locus is not accurate. The same can be said of the hydrostatic P - α approximation. The agreement for weak, partly compacted waves between the simulations and the Hugoniot locus is fortuitous. Since the crush-up pressure is small compared to the bulk modulus, the equation of state is stiff in the regime in which partly compacted waves occur. Consequently, a small change in the solid density greatly affects the stress, yet the average density is determined in large measure by the solid volume fraction. When the equilibrium volume fraction is empirically fit, the principal Hugoniot locus is insensitive to assumptions on the stress deviator.

a) $u_p = 200 \text{ m/s}$ at time = $2.0 \mu\text{s}$



b) $u_p = 500 \text{ m/s}$ at time = $1.6 \mu\text{s}$



c) $u_p = 1000 \text{ m/s}$ at time = $1.4 \mu\text{s}$

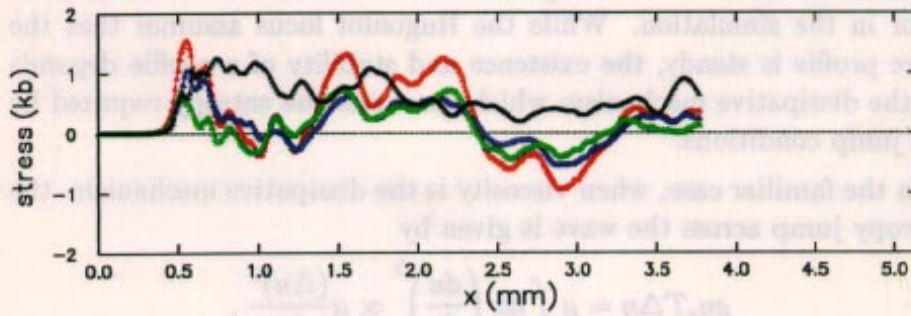


Figure 11: Profiles of components of stress deviator of compaction waves: $\sigma_{xx} - P$ in red, $P - \sigma_{yy}$ in blue, $P - \sigma_{zz}$ in green, and $|\sigma_{xy}|$ in black.

3. The velocity profiles are shown in Figs. 12 and 13. The wave profile for the x-component of the velocity is qualitatively the same as for the stress. The velocity variations are small except at the wave front. The variation at the front increases with piston velocity. For the 1000 m/s piston, the velocity of a few grains overshoots by a factor of 2. This is the expected blow-off velocity at a free surface [29] and is a consequence of the pores between grains. The re-shock when the material impacts the next grain contributes to the localized dissipation that gives rise to hot spots.

On average, the y-velocity is zero, as expected for a wave traveling in the x-direction. Immediately behind the wave front, the minimum and maximum of the transverse velocity component is a significant fraction of the piston velocity. This is due to the local rearrangement of the grains made possible by the plastic deformation that occurs when the pores are compressed out. Nesterenko [11] empirically characterized the dynamic compaction regime with a micro-kinetic energy. The micro-kinetic energy is to a large extent a measure of the extremes in the transverse velocity component at the wave front. It is a consequence rather than the cause of the pore collapse.

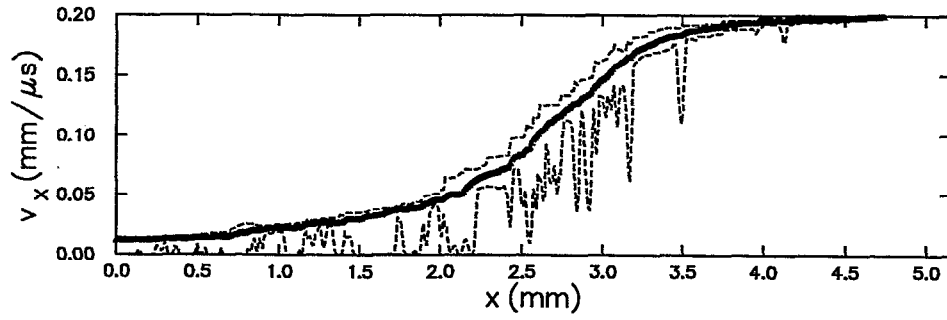
4. Energy profiles are shown in Fig. 14. The kinetic energy (green) is determined by the piston velocity. The flow behind the compaction wave has the expected value of the kinetic energy. The compaction waves are strong enough such that on the porous Hugoniot the internal energy (blue) is nearly the same as the kinetic energy. For the 200 m/s piston the internal energy in the simulation of the compaction wave exceeds the value on the Hugoniot locus. This is not necessarily an error in the simulation. While the Hugoniot locus assumes that the wave profile is steady, the existence and stability of a profile depends on the dissipative mechanism which generates the entropy required by the jump conditions.

In the familiar case, when viscosity is the dissipative mechanism, the entropy jump across the wave is given by

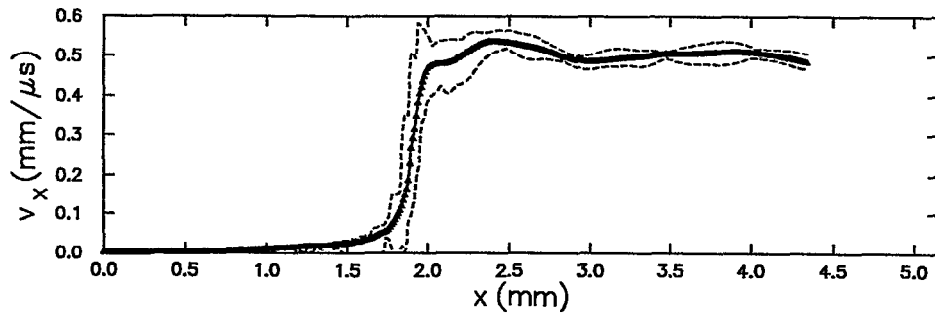
$$\rho u_s T \Delta \eta = \mu \int dx \left(\frac{du}{dx} \right)^2 \propto \mu \frac{(\Delta u)^2}{\Delta x}.$$

For any value of the viscosity coefficient μ , the width of the wave Δx can be adjusted to obtain the entropy increase $\Delta \eta$ compatible with

a) $u_p = 200 \text{ m/s}$ at time = $2.0 \mu\text{s}$



b) $u_p = 500 \text{ m/s}$ at time = $1.6 \mu\text{s}$



c) $u_p = 1000 \text{ m/s}$ at time = $1.4 \mu\text{s}$

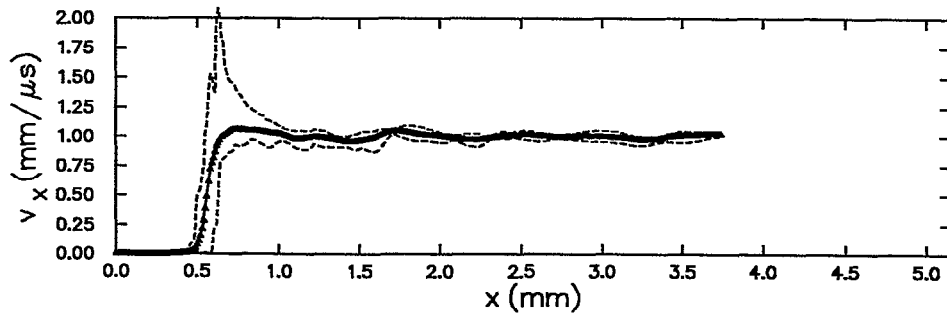
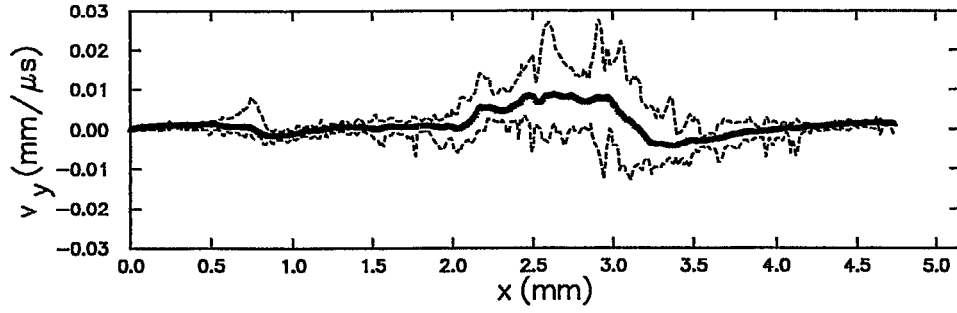
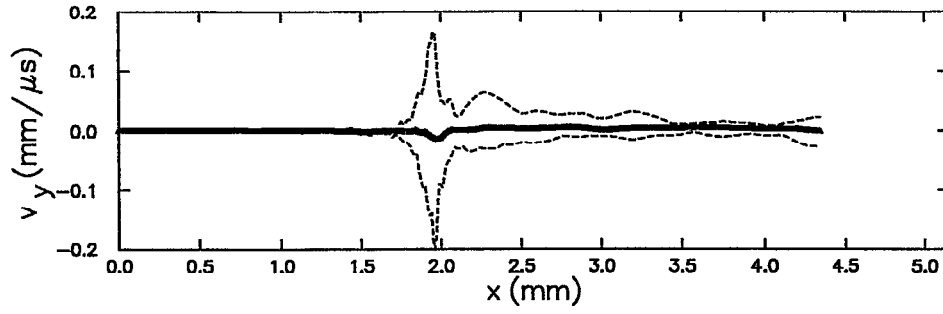


Figure 12: Velocity profile (x-component) of compaction waves.

a) $u_p = 200 \text{ m/s}$ at time = $2.0 \mu\text{s}$



b) $u_p = 500 \text{ m/s}$ at time = $1.6 \mu\text{s}$



c) $u_p = 1000 \text{ m/s}$ at time = $1.4 \mu\text{s}$

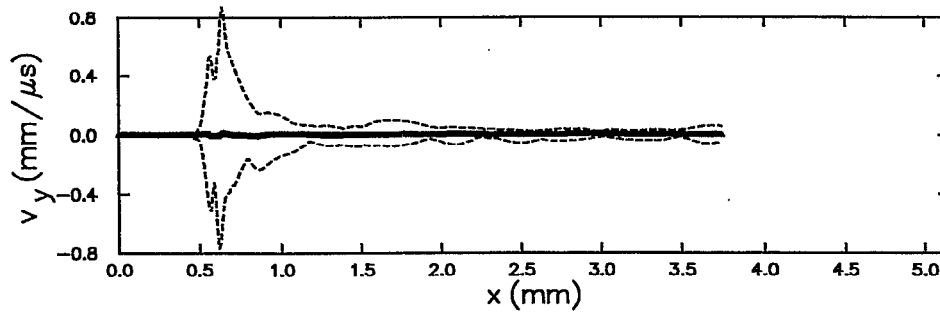


Figure 13: Velocity profile (y-component) of compaction waves.

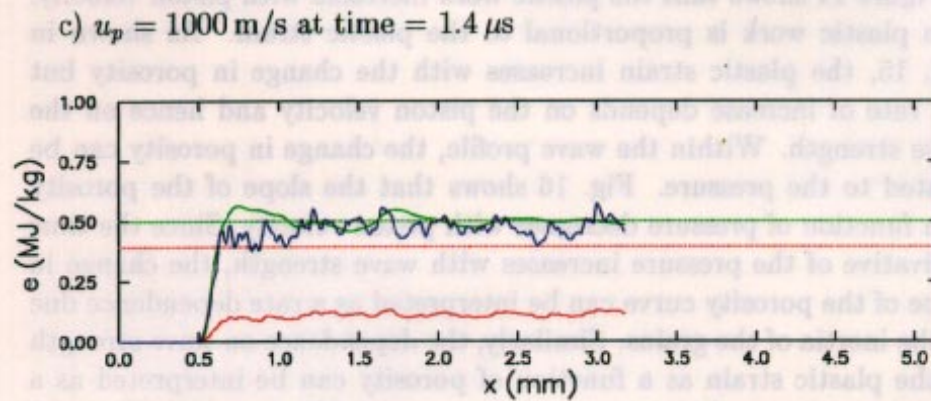
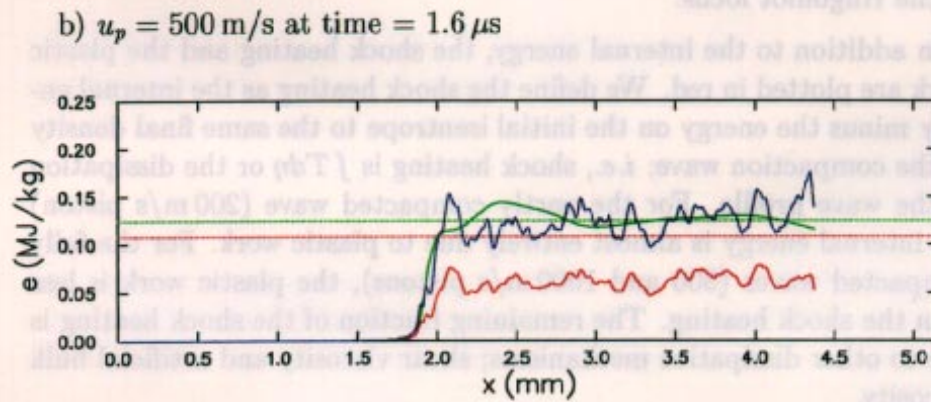
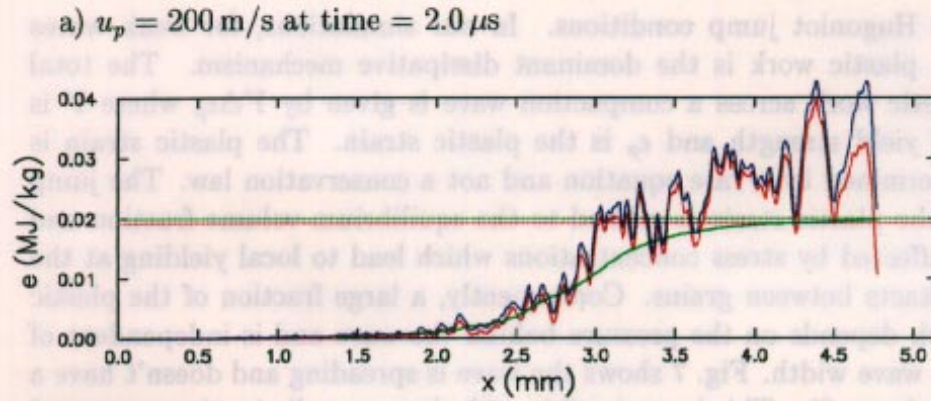


Figure 14: Energy profiles of compaction waves. Green is kinetic energy, blue is internal energy, red is plastic work. Dotted lines are corresponding values from porous Hugoniot but with red representing the shock heating. (Hugoniot kinetic energy lies on top of line for Hugoniot internal energy.)

the Hugoniot jump conditions. In our simulations, for weak waves the plastic work is the dominant dissipative mechanism. The total plastic work across a compaction wave is given by $Y\Delta\epsilon_p$ where Y is the yield strength and ϵ_p is the plastic strain. The plastic strain is determined by a rate equation and not a conservation law. The jump in the plastic strain is related to the equilibrium volume fraction and is affected by stress concentrations which lead to local yielding at the contacts between grains. Consequently, a large fraction of the plastic work depends on the pressure behind the wave and is independent of the wave width. Fig. 7 shows the wave is spreading and doesn't have a steady profile. This is compatible with the excess dissipation compared to the Hugoniot locus.

In addition to the internal energy, the shock heating and the plastic work are plotted in red. We define the shock heating as the internal energy minus the energy on the initial isentrope to the same final density as the compaction wave; *i.e.*, shock heating is $\int Td\eta$ or the dissipation in the wave profile. For the partly compacted wave (200 m/s piston) the internal energy is almost entirely due to plastic work. For the fully compacted waves (500 and 1000 m/s pistons), the plastic work is less than the shock heating. The remaining fraction of the shock heating is due to other dissipative mechanisms; shear viscosity and artificial bulk viscosity.

Figure 14 shows that the plastic work increases with piston velocity. The plastic work is proportional to the plastic strain. As shown in Fig. 15, the plastic strain increases with the change in porosity but the rate of increase depends on the piston velocity and hence on the wave strength. Within the wave profile, the change in porosity can be related to the pressure. Fig. 16 shows that the slope of the porosity as a function of pressure decreases with piston velocity. Since the time derivative of the pressure increases with wave strength, the change in slope of the porosity curve can be interpreted as a rate dependence due to the inertia of the grains. Similarly, the dependence on wave strength of the plastic strain as a function of porosity can be interpreted as a rate dependence of the compaction process. We note that the rate dependence of the porosity is not included in the P - α model but is included in the closely related single-phase limit of the Baer-Nunziato model [30].

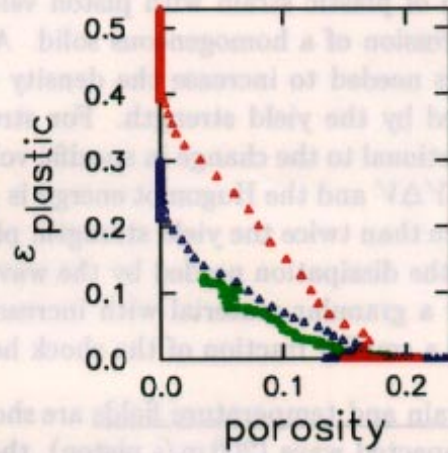


Figure 15: Porosity vs. plastic strain on the wave profile. Wave profile has been smoothed by taking a running average over a distance of 1 grain diameter (0.14 mm). Green, blue and red correspond to piston velocities of 200, 500 and 1000,m/s, respectively.

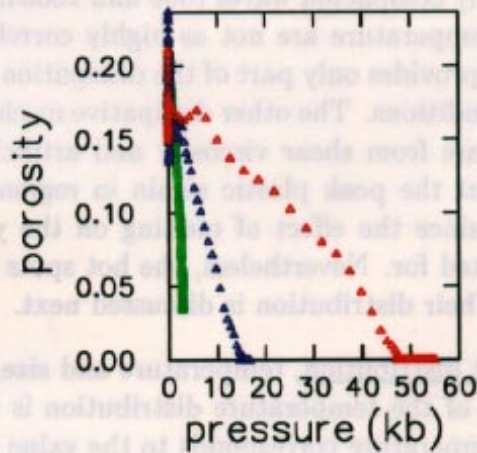


Figure 16: Porosity vs. pressure on the wave profile. Wave profile has been smoothed by taking a running average over a distance of 1 grain diameter (0.14 mm). Green, blue and red correspond to piston velocities of 200, 500 and 1000,m/s, respectively.

The increase of plastic strain with piston velocity has an analog in uniaxial compression of a homogeneous solid. Above the elastic limit, plastic strain is needed to increase the density since the elastic shear strain is limited by the yield strength. For strong waves, the plastic strain is proportional to the change in specific volume. Since the plastic work is $\epsilon_p Y \sim Y \Delta V$ and the Hugoniot energy is $\frac{1}{2} P \Delta V$, when the wave pressure is more than twice the yield strength, plastic work can provide only a part of the dissipation needed by the wave. Similarly, Figure 14 shows that for a granular material with increasing wave strength the plastic work is a smaller fraction of the shock heating.

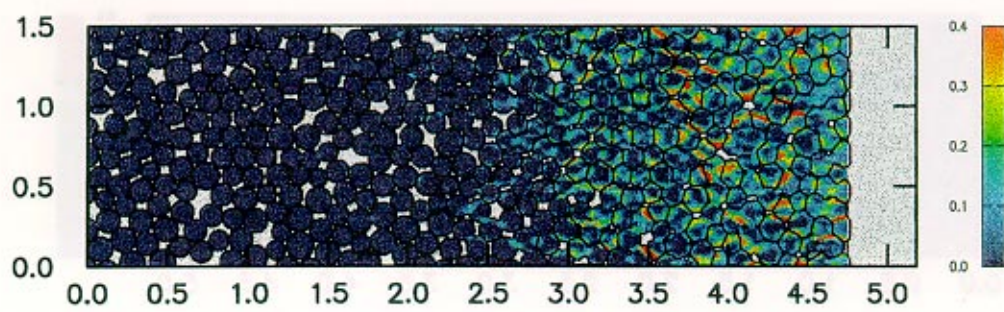
5. The plastic strain and temperature fields are shown in Figs. 17-19. For the partly compacted wave (200 m/s piston), the high temperature regions correspond to the regions of large plastic strain. This is expected since the internal energy is almost entirely due to plastic work. Moreover, large plastic strains result from deformations due to stress concentrations at the contact surfaces between grains. Consequently, hot spots occur in regions near grain interfaces.

For the fully compacted waves (500 and 1000 m/s pistons) the plastic strain and temperature are not as highly correlated. This is because plastic work provides only part of the dissipation required by the Hugoniot jump conditions. The other dissipative mechanisms included in the simulations are from shear viscosity and artificial bulk viscosity. We also note that the peak plastic strain in regions of high deformation is excessive since the effect of melting on the yield strength has not been accounted for. Nevertheless, the hot spots still occur along grain interfaces. Their distribution is discussed next.

6. The hot-spot distribution, temperature and size, are shown in Fig. 20. The average of the temperature distribution is the bulk temperature. The bulk temperature corresponds to the value on the Hugoniot locus and is close to the temperature with the peak value of the mass fraction. Since the hot spots are above the average, some material must be at temperatures below the Hugoniot temperature. The low temperatures correspond to the interior of the grains.

From the plot of induction time shown in Fig. 4, a hot spot with a temperature of 650 to 700 K burns within about one μs . For the 1000 m/s piston, the bulk temperature of 720 K is sufficient to lead

a) Plastic strain



b) Temperature

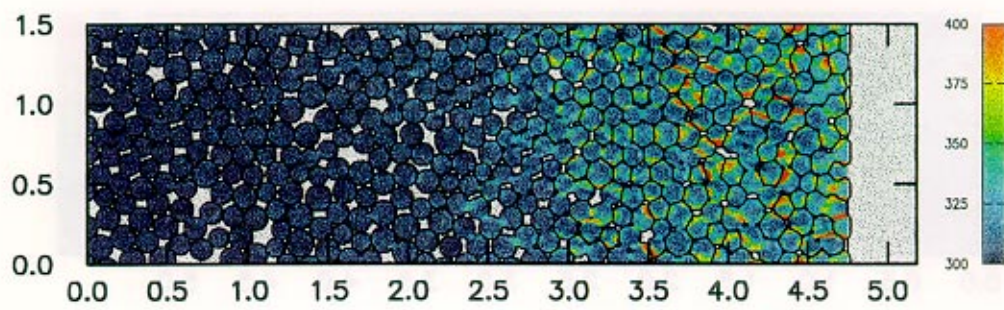
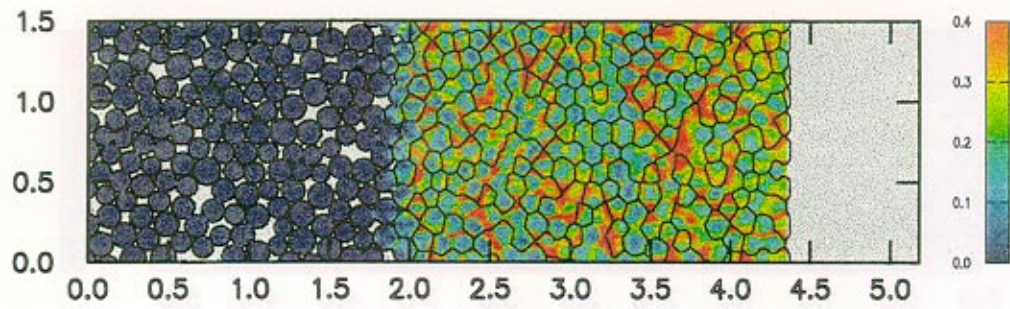


Figure 17: Plastic strain and temperature for 200 m/s piston at time = 2.0 μs .

a) Plastic strain



b) Temperature

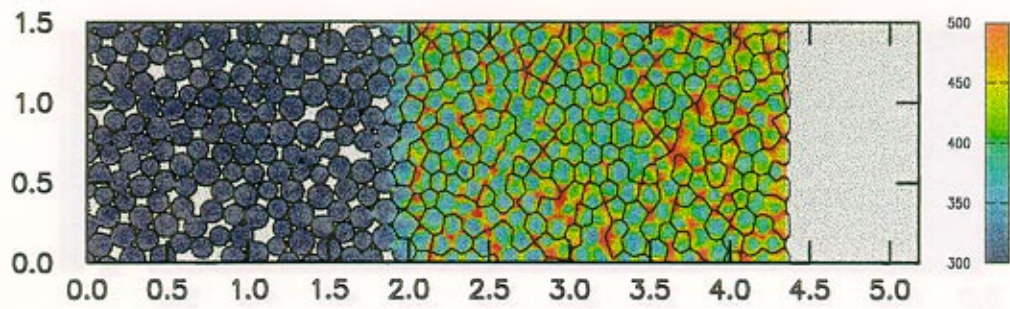
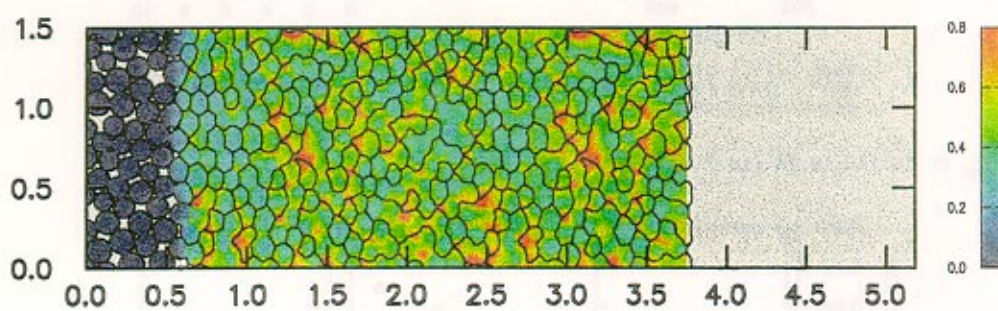


Figure 18: Plastic strain and temperature for 500 m/s piston at time = 1.6 μs .

a) Plastic strain



b) Temperature

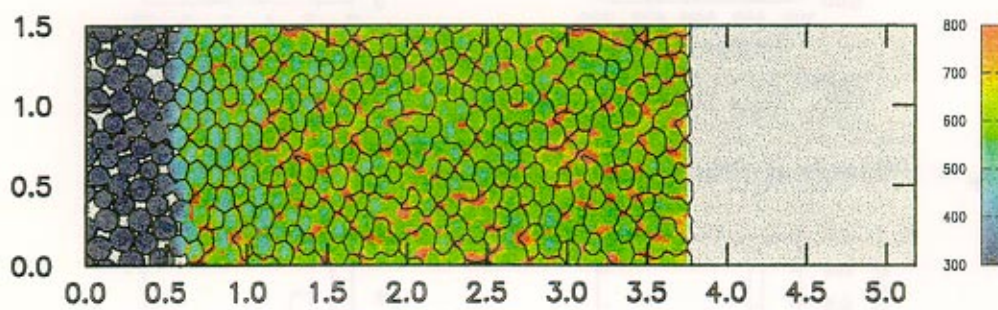
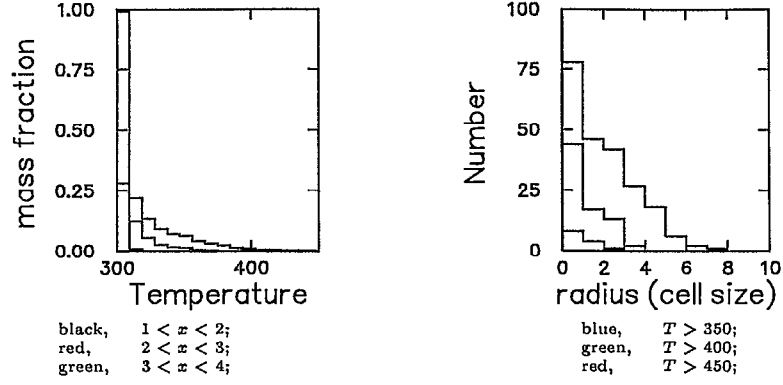
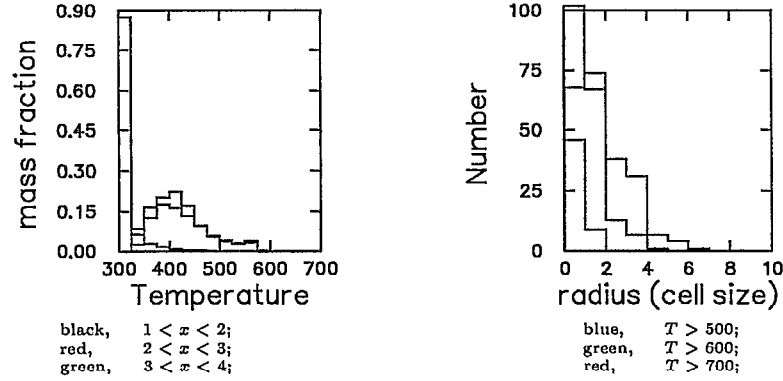


Figure 19: Plastic strain and temperature for 1000 m/s piston at time = 1.4 μ s.

a) $u_p = 200 \text{ m/s}$ at time = $2.0 \mu\text{s}$



b) $u_p = 500 \text{ m/s}$ at time = $1.6 \mu\text{s}$



c) $u_p = 1000 \text{ m/s}$ at time = $1.4 \mu\text{s}$

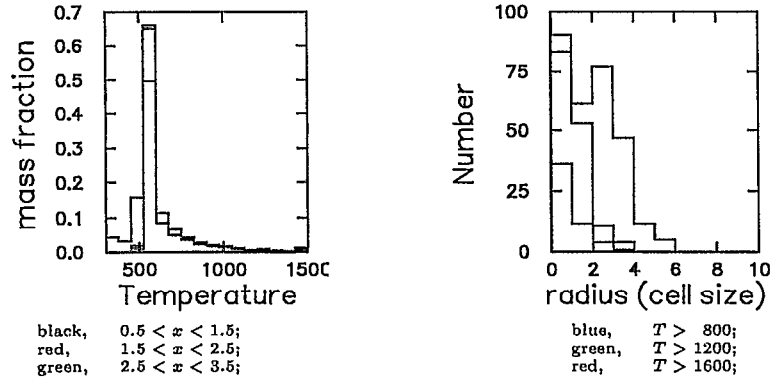
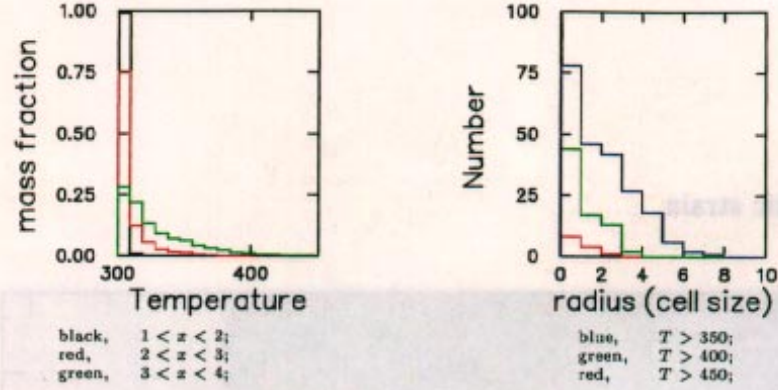
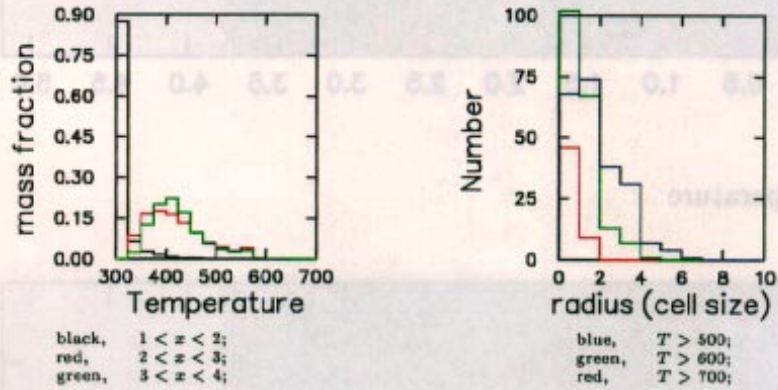


Figure 20: Temperature distribution and hot-spot area. Area is specified by the radius of an equivalent circle. Cell radius is $10 \mu\text{m}$. Initial grain radius is 7 cells.

a) $u_p = 200 \text{ m/s}$ at time = $2.0 \mu\text{s}$



b) $u_p = 500 \text{ m/s}$ at time = $1.6 \mu\text{s}$



c) $u_p = 1000 \text{ m/s}$ at time = $1.4 \mu\text{s}$

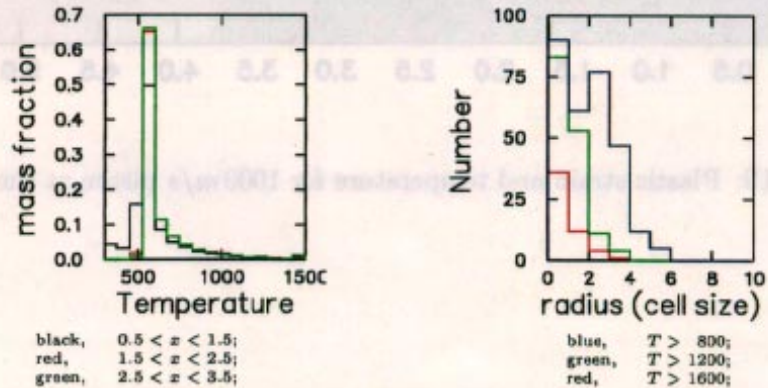


Figure 20: Temperature distribution and hot-spot area. Area is specified by the radius of an equivalent circle. Cell radius is $10 \mu\text{m}$. Initial grain radius is 7 cells.

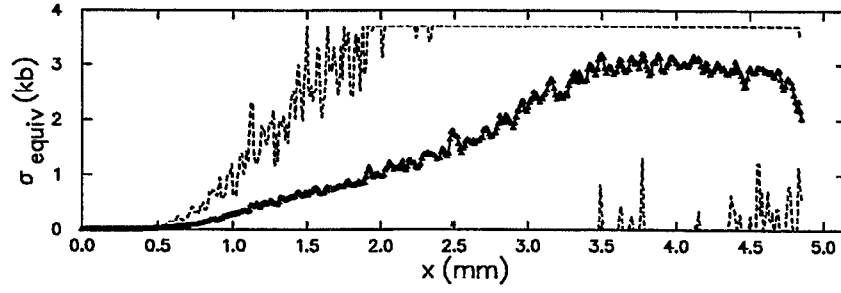
to prompt ignition. For the weaker compaction waves, the tail of the temperature distribution is within a range that will cause significant reaction and the hot spots can be expected to lead to a delayed ignition. In fact, detonation waves are observed to occur after about $100\ \mu\text{s}$ in DDT tube experiments driven by a piston with a velocity of about $200\ \text{m/s}$. Gas gun experiments corresponding to piston velocities of $500\ \text{m/s}$ show significant burning occurs after the compaction wave propagates only a few mm. Our simulations are compatible with these results.

However, the resolution of our simulations is limited. The highest temperatures occur within hot spots of only 1 or 2 cells in extent, red curve in Fig. 20. Very likely these temperatures are affected by numerical errors at grain interfaces. Computed hot spots with a larger size, green curve in Fig. 20, are likely to have smaller error bars. Because of the uncertainty in the temperature distribution for the simulation, the computed mass-averaged reaction rate is subject to large errors. Qualitatively, the simulations do show that the hot spots are within the range expected to have a significant effect on ignition. Higher resolution would be needed for quantitative predictions of the reaction rate.

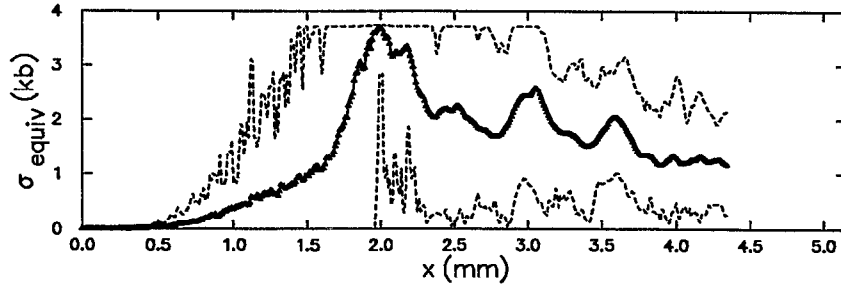
7. The equivalent plastic stress and plastic strain are shown in Figs. 21 and 22. With the von Mises yield condition, plastic flow occurs when the equivalent plastic stress ($\sqrt{\frac{3}{2}} \|\sigma'\|$) equals the yield strength. Furthermore, for rate independent plasticity the equivalent stress is limited to the yield stress. As a result the equivalent stress is a convenient quantity for examining the elastic precursor in weak compaction waves.

The leading edge of the precursor is at the same position ($\approx 0.5\ \text{mm}$ at $t = 1.6\ \mu\text{s}$) for both the 200 and $500\ \text{m/s}$ piston. The precursor velocity is 2.9 to $3.0\ \text{mm}/\mu\text{s}$. This is to be compared to the solid longitudinal sound speed of $c_{\text{long}} = 3.75\ \text{mm}/\mu\text{s}$, and the bulk sound speed of $c_{\text{bulk}} = 2.65\ \text{mm}/\mu\text{s}$. It appears that the precursor speed is about $\phi_0 c_{\text{long}} = 3.0\ \text{mm}/\mu\text{s}$. The porosity is expected to lower the acoustic speed since a wave is transmitted from one grain to the next only through the contact surfaces. Hence, the effective path length the wave travels is longer and the average speed is lower. But we have no theory for the form given above.

a) $u_p = 200 \text{ m/s}$ at time = $1.6 \mu\text{s}$



b) $u_p = 500 \text{ m/s}$ at time = $1.6 \mu\text{s}$



c) $u_p = 1000 \text{ m/s}$ at time = $1.4 \mu\text{s}$

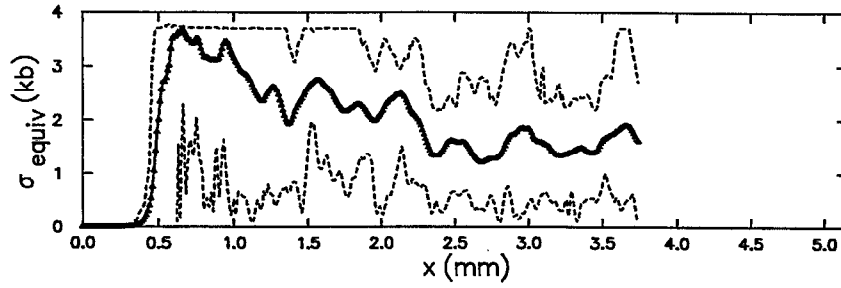


Figure 21: Equivalent plastic stress $\left(\left(\frac{3}{2} \right)^{\frac{1}{2}} \|\sigma'\| \right)$ profile of compaction waves. Plastic yield occurs at 3.7kb.

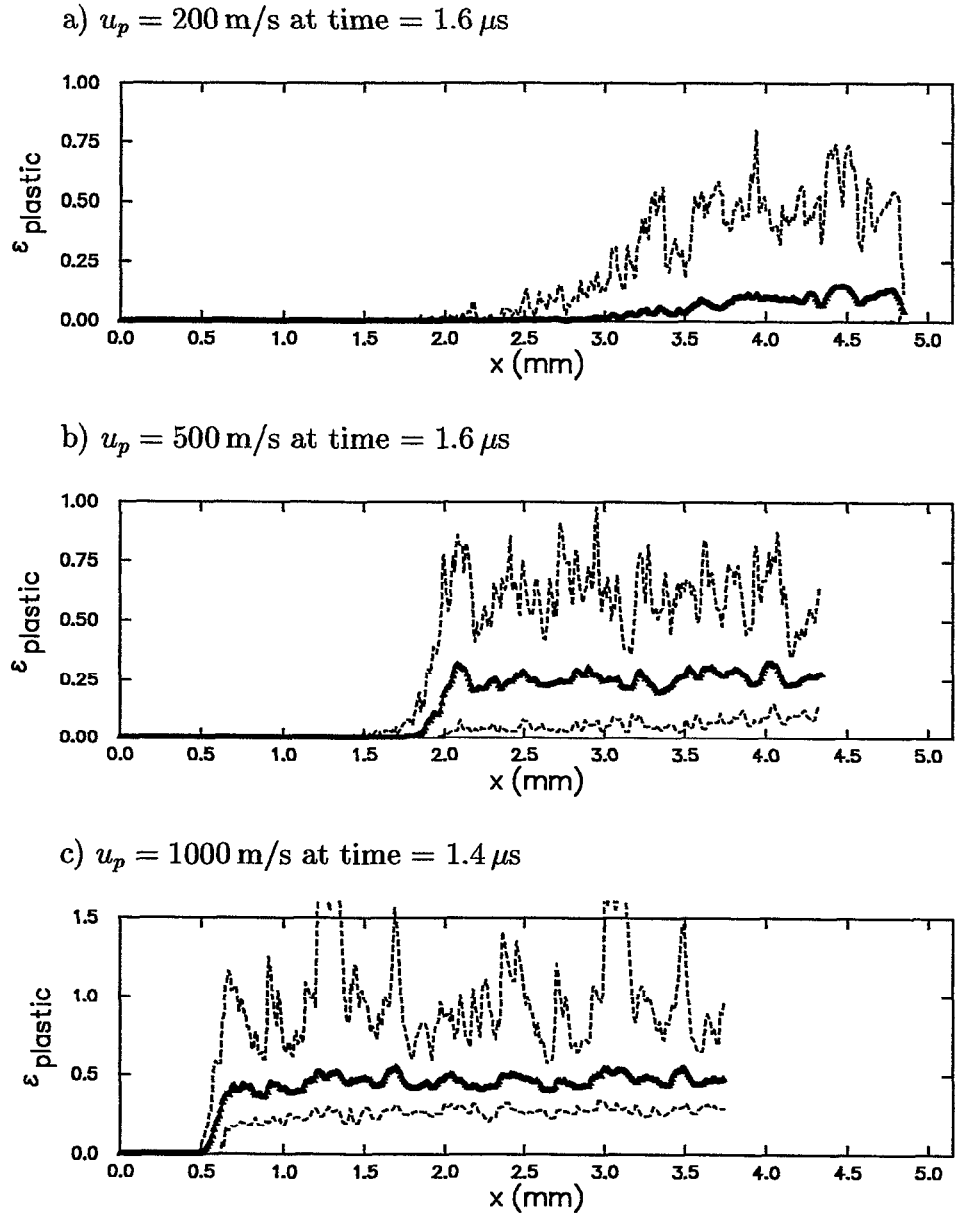


Figure 22: Plastic strain of compaction waves.

For the 1000 m/s piston, the wave speed ($3.4 \text{ mm}/\mu\text{s}$) exceeds the precursor speed. Consequently, the plastic wave outruns the elastic wave, and a precursor is not possible. Thus, the precursor behavior is similar to that of the pure solid. However, in contrast to a split wave as shown in Fig. 2, the elastic-plastic transition gives rise to a highly dispersed precursor.

The profiles of equivalent stress and plastic strain show the effect of stress concentrations. Localized yielding occurs when the profile of the maximum equivalent stress reaches the yield strength. In fact, the position of the plastic wave in Fig. 8 coincides with the rapid rise in the average plastic strain. Plastic strain is needed to change the porosity, as shown in Fig. 15. Consequently, the plastic wave corresponds to changes in porosity, variation of porosity with pressure shown in Fig. 16, and the precursor results from the elastic behavior.

However, the precursor is not purely elastic. Even with a small average stress, localized stress concentrations give rise to a small amount of plastic strain and hence dissipation. Because of the limited resolution, as discussed Subsection 4.2, the simulations underestimate the dissipation in the precursor. Consequently, we expect the precursor to damp faster than the calculations predict.

For a homogeneous solid, weak waves below the Hugoniot elastic limit correspond to elastic shocks. In contrast, weak waves in a porous solid would correspond to the precursor we have been discussing. They would display substantial stress fingering and spread out in time rather than having the form of a traveling wave. Consequently, a key assumption used to calculate the porous Hugoniot in Section 3 is violated for weak waves (below the yield strength, an average stress of say 1 kb). Furthermore, the stress fingering raises the stress concentrations and would cause plastic deformation to occur at a lower wave stress than the elastic limit given in Table 5. Due to the small contact surfaces at which plastic deformation occurs, high resolution would be required to calculate accurately the dissipation in weak waves.

Though the pure solid is perfectly plastic and rate independent, the average behavior of a granular bed does not inherit these properties. Profiles in the plastic (stress, strain)-plane are shown in Fig. 23. These profiles have been smoothed by taking a running average over a length

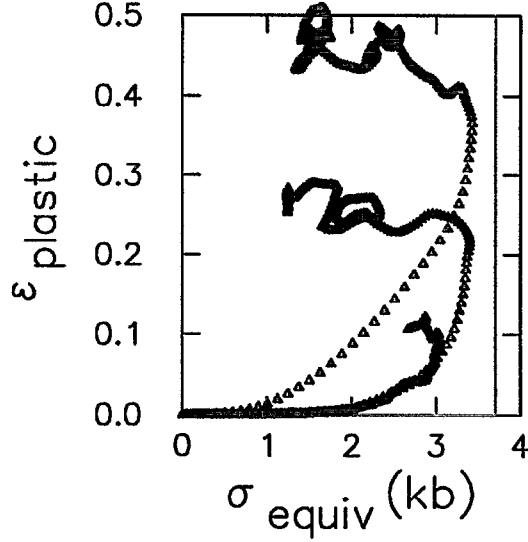


Figure 23: Effective plastic behavior. Average profiles of 200 m/s piston in red, 500 m/s piston in blue and 1000 m/s in green. Solid green line is for perfectly plastic pure solid.

of one grain diameter. The smooth increase in the plastic strain with equivalent stress corresponds to the stress rise in the wave profile. The decrease in the equivalent stress occurs behind the wave front. It is a consequence of the relaxation of the components of the stress deviator shown in Fig. 11. The final equivalent stress is nearly the same for the 500 and 1000 m/s piston. The length of run for the 200 m/s piston may not be long enough for relaxation to occur.

This average behavior of the granular HMX bed is suggestive of rate dependent plasticity. Work hardening would be needed if the asymptotic value of the equivalent stress varied with plastic strain. Longer runs would be needed to determine these asymptotic values. For a model based on the average material behavior it would be more appropriate to use $||\langle\sigma\rangle'||$ rather than $\langle||\sigma'||||$. Both measures of the average equivalent stress display a similar relaxation effect.

The results to this point can be summarized as follows. The mechanical properties of a compaction wave in a granular bed, stress and wave speed, are in good agreement with the porous Hugoniot locus for uniaxial-strain.

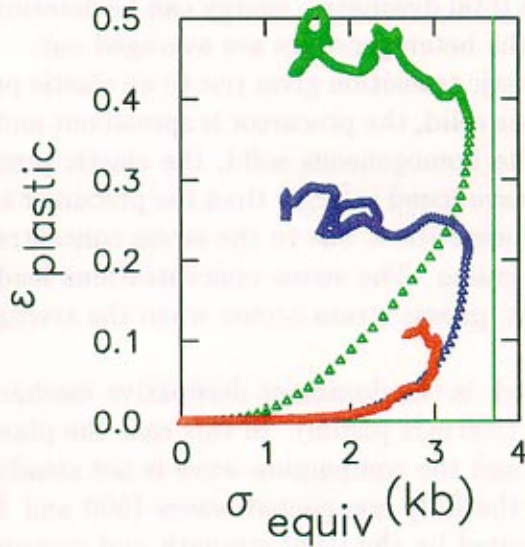


Figure 23: Effective plastic behavior. Average profiles of 200 m/s piston in red, 500 m/s piston in blue and 1000 m/s in green. Solid green line is for perfectly plastic pure solid.

of one grain diameter. The smooth increase in the plastic strain with equivalent stress corresponds to the stress rise in the wave profile. The decrease in the equivalent stress occurs behind the wave front. It is a consequence of the relaxation of the components of the stress deviator shown in Fig. 11. The final equivalent stress is nearly the same for the 500 and 1000 m/s piston. The length of run for the 200 m/s piston may not be long enough for relaxation to occur.

This average behavior of the granular HMX bed is suggestive of rate dependent plasticity. Work hardening would be needed if the asymptotic value of the equivalent stress varied with plastic strain. Longer runs would be needed to determine these asymptotic values. For a model based on the average material behavior it would be more appropriate to use $\|\langle \sigma \rangle'\|$ rather than $\langle \|\sigma'\| \rangle$. Both measures of the average equivalent stress display a similar relaxation effect.

The results to this point can be summarized as follows. The mechanical properties of a compaction wave in a granular bed, stress and wave speed, are in good agreement with the porous Hugoniot locus for uniaxial-strain.

Consequently, the total dissipative energy can be determined from continuum models in which the heterogeneities are averaged out.

The elastic-plastic transition gives rise to an elastic precursor. In contrast to the homogeneous solid, the precursor is spread out and not a discontinuous shock. As with the homogeneous solid, the elastic precursor is not present when the plastic wave speed is larger than the precursor speed. The spreading out of the elastic precursor is due to the stress concentrations at the contact surfaces between grains. The stress concentrations lead to localized plastic deformation. Thus, plastic strain occurs when the average stress is below the yield strength.

The plastic work is the dominant dissipative mechanism for weak partly compacted waves (200 m/s piston). In this case the plastic work exceeds the Hugoniot energy, and the compaction wave is not steady; instead, it spreads out in time. For the fully compacted waves (500 and 1000 m/s piston) the plastic work is limited by the yield strength and comprises only part of the shock heating.

The granular heterogeneities give rise to fluctuations in the temperature. Homogenization theories typically account for only the average effect of fluctuations. This is a reasonable approximation for inert materials, but not for reacting materials with temperature sensitive reaction rates. For the compaction waves in our simulations, the fluctuations are in a range that would have a critical effect on ignition sensitivity. However, the fluctuations depend on mesh resolution and the assumed dissipative mechanisms in the constitutive model. The sensitivities to yield strength and shear viscosity are discussed in the next subsections.

5.2 Effect of Yield Strength

Material strength allows the granular bed to have a non-zero porosity under stress. The stress above which a pore must collapse, often referred to as the crush-up pressure, determines the wave strength to achieve a fully compacted wave, *i.e.*, $\phi = 1$ behind the wave. Assuming the pores between grains are voids, a non-zero porosity requires that the normal component of the stress vanishes along grain-pore interfaces. Consequently, the maximum eigenvalue of the stress tensor subject to the condition that another eigenvalue vanishes provides an estimate for the crush-up pressure. Since we are interested in compaction waves, the maximum stress component, rather than the pressure, is a good criterion for pore collapse. The crush-up stress has

a dependence on dimensionality. We estimate it in both 2-D (planar-strain) and in 3-D.

For the estimate it is sufficient to consider the case in which the stress and strain tensors are diagonal. In 2-D, the planar strain tensor has the form

$$\epsilon = \frac{1}{3}\text{diag}(\epsilon, \epsilon, \epsilon) + \frac{1}{3}\text{diag}(\epsilon_1, \epsilon - \epsilon_1, -\epsilon) ,$$

in which the third component of strain vanishes. The corresponding stress tensor, assuming linear elasticity, has the form

$$\sigma = K\text{diag}(\epsilon, \epsilon, \epsilon) + \frac{2G}{3}\text{diag}(\epsilon_1, \epsilon - \epsilon_1, -\epsilon) ,$$

where K is the bulk modulus and G is the shear modulus. Requiring the second component of the stress to be zero gives

$$\epsilon_1 = \left(\frac{3K}{2G} + 1 \right) \epsilon .$$

Von Mises yield condition then determines ϵ

$$Y^2 = \frac{3}{2}\|\sigma'\|^2 = \frac{2}{3} \left[\left(\frac{3}{2}K + G \right)^2 + \left(\frac{3}{2}K \right)^2 + G^2 \right] \epsilon^2 ,$$

where Y is the yield strength. After some algebra, the maximum stress component can be expressed as

$$\sigma_{xx} = \left(1 - \nu + \nu^2 \right)^{-\frac{1}{2}} Y , \quad (17)$$

where ν is the Poisson ratio. For HMX, $\nu = 0.2$ and a wave with a stress, $\sigma_{xx} > 1.09Y$, will be fully compacted. With $Y = 3.7\text{kb}$, a wave driven by a 200 m/s piston has a stress slightly below the value needed for full compaction. However, stress fluctuations due to the granular heterogeneities can lead to a small amount of porosity at our estimated crush-up stress which is based only on local conditions.

In 3-D, a similar analysis leads to a maximum stress component at crush-up of

$$\sigma_{xx} = \frac{2}{\sqrt{3}}Y \approx 1.15Y . \quad (18)$$

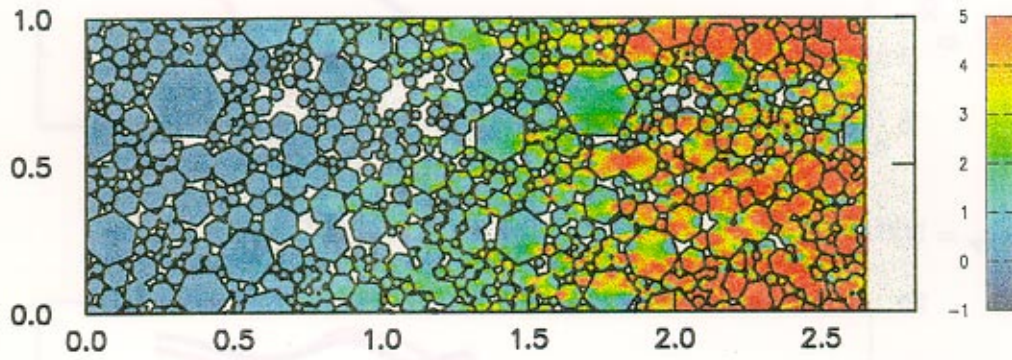
The 3-D maximum stress is greater than the 2-D maximum stress since it is not limited by the constraint of planar strain. However, for HMX the maximum stress is only 5% larger in 3-D than in 2-D.

To show the effect of yield strength on a compaction wave, simulations were run with a high and low value of the yield strength; 3.7 and 0.48 kb respectively. The stress fields and stress profiles are compared in Figs. 24 and 25. These simulations used hexagonal grains with a log-normal size distribution on a 564×200 mesh with $5 \mu\text{m}$ cells.

Yield strength has a considerable effect on weak compaction waves. For the 200 m/s piston, with the low yield strength the stress is above the crush-up pressure, and the wave is fully compacted; *i.e.*, $\phi = 1$ behind the wave front. While in the high yield strength case, the stress is slightly below the estimated crush-up pressure, and the wave is partly compacted. Fig. 25 shows that the wave speed and the final stress are different. This is a consequence of the different final porosities. The mass, momentum and energy jump conditions must be supplemented with the equilibrium porosity to determine the Hugoniot locus. The equilibrium porosity in turn is a function of the yield strength. Moreover, it can be shown that decreasing the porosity has a similar effect to an endothermic reaction in that the partial Hugoniots with fixed ϕ are shifted to the left in the (V, P) -plane. Though it may seem counter intuitive, for fixed piston velocity the stress and wave speed decrease with a lower yield strength as observed in the simulations. For the 500 m/s piston, both cases are fully compacted, and the final stress and wave speed are nearly the same.

The lower yield strength has two other effects. It sets the stress scale for the elastic precursor. In particular, the steep gradient associated with the plastic wave starts at a stress of about the yield strength. The experimental rise time for a compaction wave is typically estimated as the time between 5% and 95% of the maximum on the profile. Hence decreasing the precursor can change the estimate of the rise time. The rise time for the weak partly compacted wave in the simulation with the expected value of the yield strength is larger than that observed in gas gun experiments, see [9, Figs. 2.8 and 2.9], even after correcting for differences in porosity and grain size. A yield criterion with work hardening would have a large effect on the precursor and hence the rise time of the compaction wave. Physically this is quite plausible for the following reasons: (i) HMX twins at low stress, but the accumulation of defects limits the amount of twinning [16], and (ii) quasi-static hardness measurements lead to an estimate of the yield strength of 0.13 GPa [31], which is factor of 2.5 lower than the value obtained from dynamic wave profiles [14]. The precursor has a smaller effect for stronger fully compacted waves.

a) $Y = 3.7 \text{ kb}$



b) $Y = 0.48 \text{ kb}$

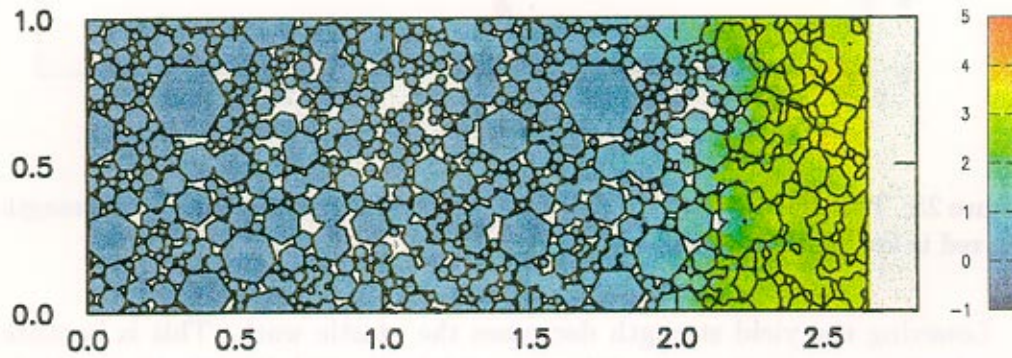
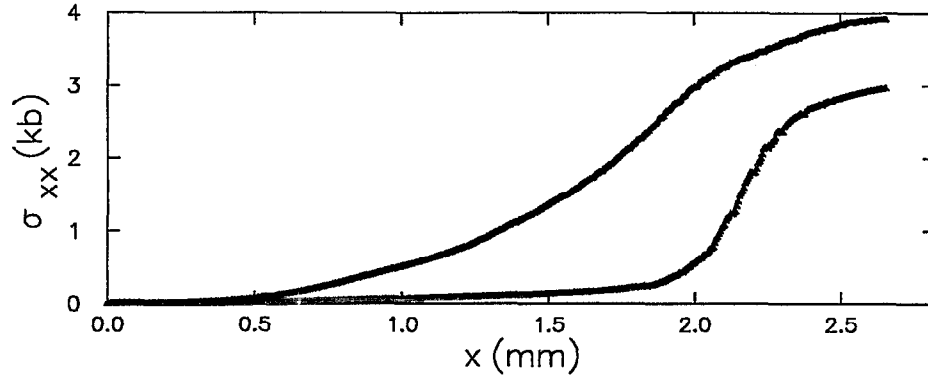


Figure 24: The effect of yield strength on stress σ_{xx} . Simulations apply a 200 m/s piston to a bed composed of hexagonal grains with log-normal grain size distribution. The plots are at a time of $0.8 \mu\text{s}$ and the mesh had cell size of $5 \mu\text{m}$.

a) $u_p = 200 \text{ m/s}$



b) $u_p = 500 \text{ m/s}$

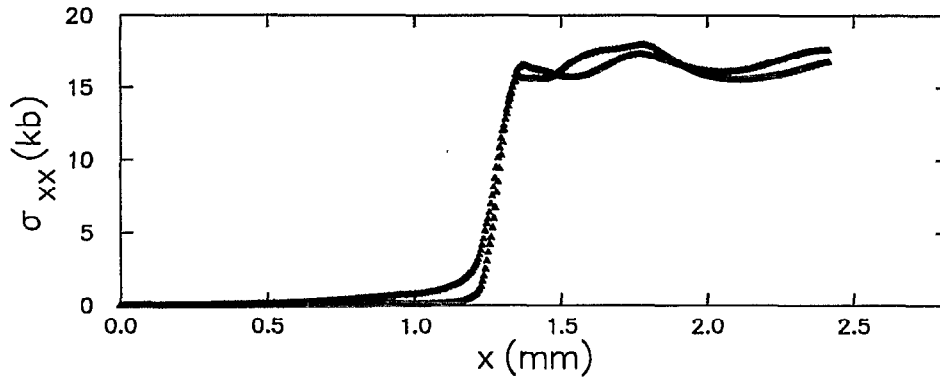
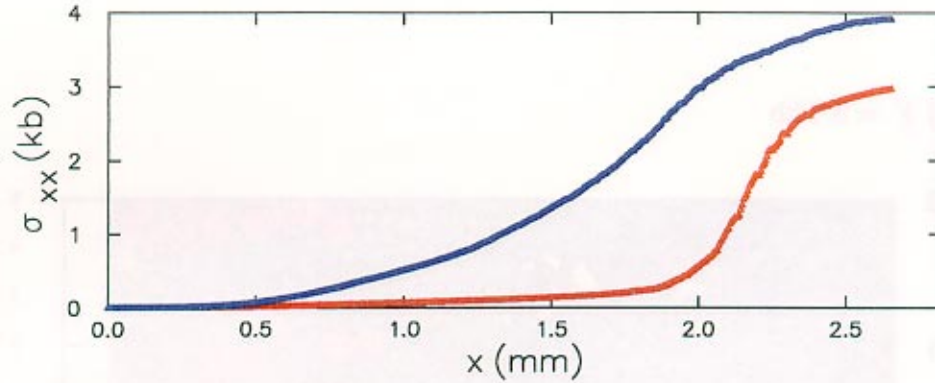


Figure 25: The effect of yield strength on stress profiles: blue is high yield strength and red is low yield strength.

Lowering the yield strength decreases the plastic work. This is because the plastic work is given by (plastic strain) \times Y , and the plastic strain is related to the change in porosity. Consequently, the yield strength affects the proportion of shock heating due to plastic deformation. Changing the dissipative mechanisms for shock heating in turn affects the distribution of hot spots. For the 500 m/s piston, Fig. 26 shows that the hot-spot mass increases with yield strength.

The high yield cases here correspond to those in the previous subsection, except for the grain size distribution. Both cases have an initial porosity of

a) $u_p = 200 \text{ m/s}$



b) $u_p = 500 \text{ m/s}$

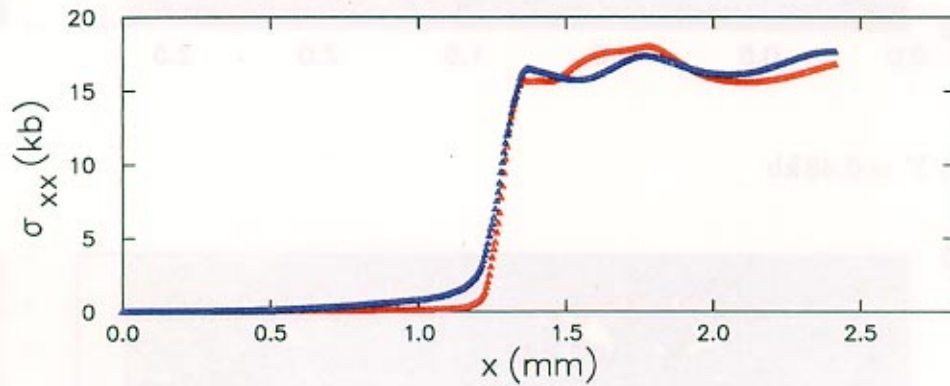


Figure 25: The effect of yield strength on stress profiles: blue is high yield strength and red is low yield strength.

Lowering the yield strength decreases the plastic work. This is because the plastic work is given by (plastic strain) \times Y , and the plastic strain is related to the change in porosity. Consequently, the yield strength affects the proportion of shock heating due to plastic deformation. Changing the dissipative mechanisms for shock heating in turn affects the distribution of hot spots. For the 500 m/s piston, Fig. 26 shows that the hot-spot mass increases with yield strength.

The high yield cases here correspond to those in the previous subsection, except for the grain size distribution. Both cases have an initial porosity of

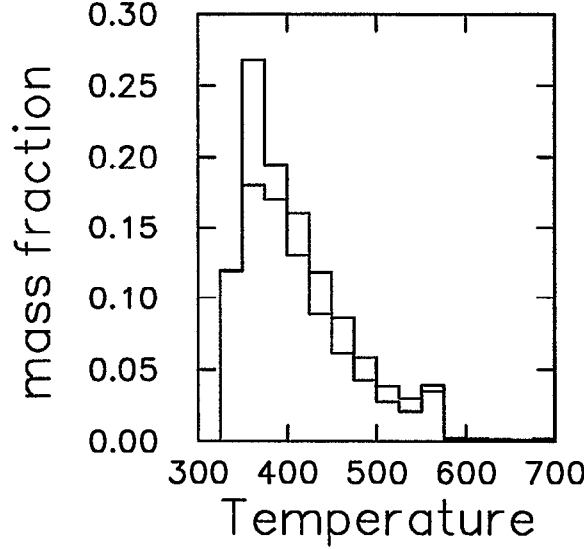


Figure 26: Comparison of hot-spot distribution behind wave front ($1.5 < x < 2$) with yield strength for 500 m/s piston: blue is high yield strength and red is low yield strength.

19%. It is noteworthy from comparing Fig. 9a with Fig. 24a and Fig. 8a with Fig. 25a that the mechanical structure of a compaction wave does not appear sensitive to the grain size distribution. Both cases display stress fingering, and the average stress behind the wave is about the same. Even the leading edge of the elastic precursor has the same velocity. The mono-dispersed distribution allowed for a larger cell size and a longer distance of run. We had expected the sharp corners in the hexagonal grains to cause greater plastic distortion and lead to higher hot-spot temperatures. This effect was not observed. We now believe the calculations do not have sufficient resolution per grain to determine whether such an effect exists.

Up to this point the simulations have used a constant yield strength. However, the yield strength and the shear modulus should vanish when the grains melt. To determine the magnitude of this effect additional simulations were run with the mono-dispersed granular bed. A comparison of the plastic strain profiles for a 1000 m/s piston is shown in Fig. 27. As expected, melting limits the plastic strain. The corresponding temperature distributions are shown in Fig. 28. Melting broadened the distribution around the peak but hardly affected the tail. This is a consequence of the energy profiles in Fig. 14, which

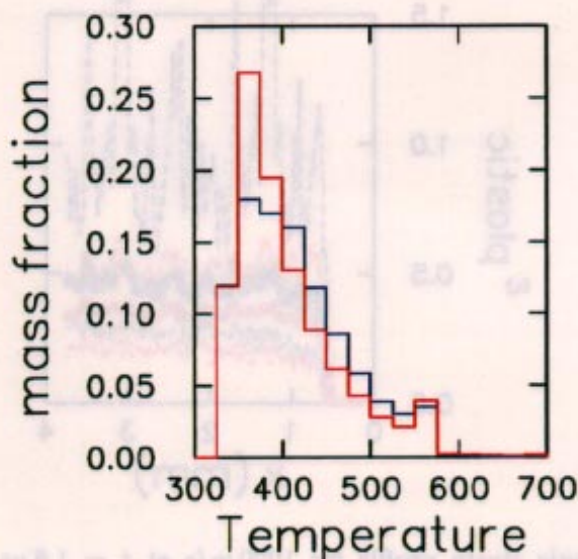


Figure 26: Comparison of hot-spot distribution behind wave front ($1.5 < x < 2$) with yield strength for 500 m/s piston: blue is high yield strength and red is low yield strength.

19%. It is noteworthy from comparing Fig. 9a with Fig. 24a and Fig. 8a with Fig. 25a that the mechanical structure of a compaction wave does not appear sensitive to the grain size distribution. Both cases display stress fingering, and the average stress behind the wave is about the same. Even the leading edge of the elastic precursor has the same velocity. The mono-dispersed distribution allowed for a larger cell size and a longer distance of run. We had expected the sharp corners in the hexagonal grains to cause greater plastic distortion and lead to higher hot-spot temperatures. This effect was not observed. We now believe the calculations do not have sufficient resolution per grain to determine whether such an effect exists.

Up to this point the simulations have used a constant yield strength. However, the yield strength and the shear modulus should vanish when the grains melt. To determine the magnitude of this effect additional simulations were run with the mono-dispersed granular bed. A comparison of the plastic strain profiles for a 1000 m/s piston is shown in Fig. 27. As expected, melting limits the plastic strain. The corresponding temperature distributions are shown in Fig. 28. Melting broadened the distribution around the peak but hardly affected the tail. This is a consequence of the energy profiles in Fig. 14, which

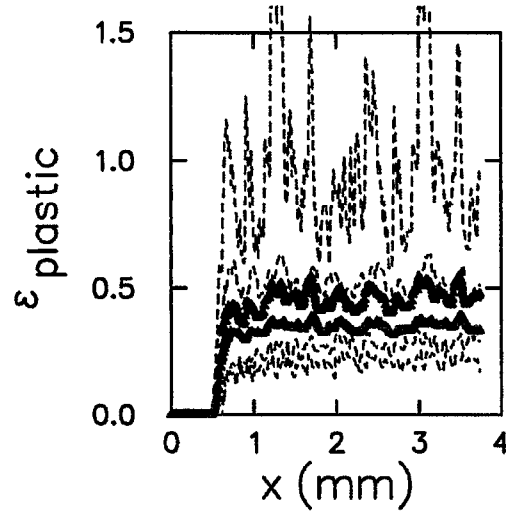


Figure 27: Plastic strain profile for 1000 m/s at $t = 1.6 \mu\text{s}$ with and without melting. Blue is standard case with constant yield strength. Red is case in which yield strength vanishes above melting temperature. Line with symbols represents the average. Dashed lines represent the minimum and maximum.

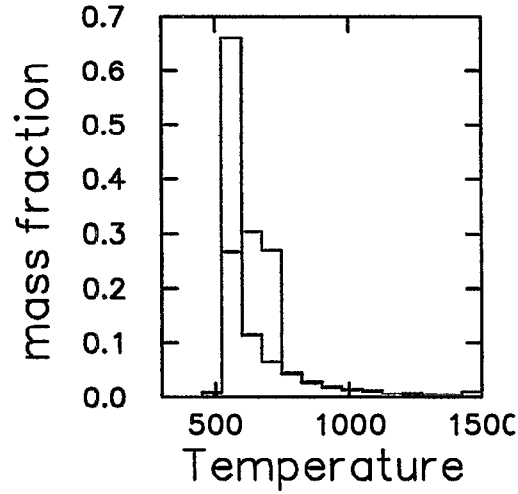


Figure 28: Effect of lowering yield strength above melting on hot-spot distribution for 1000 m/s piston. Blue is standard case with constant yield strength. Red is case in which yield strength vanishes above melting temperature.

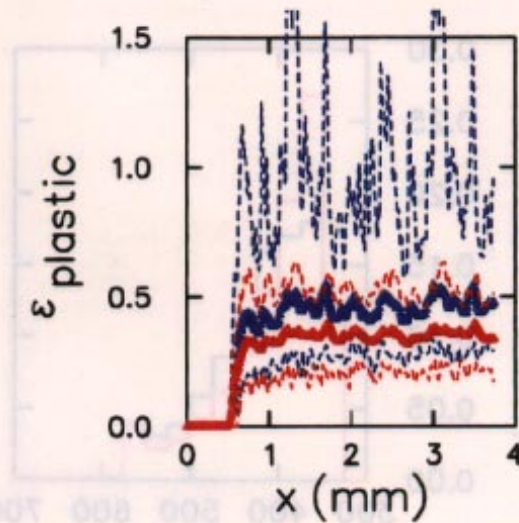


Figure 27: Plastic strain profile for 1000 m/s at $t = 1.6 \mu\text{s}$ with and without melting. Blue is standard case with constant yield strength. Red is case in which yield strength vanishes above melting temperature. Line with symbols represents the average. Dashed lines represent the minimum and maximum.

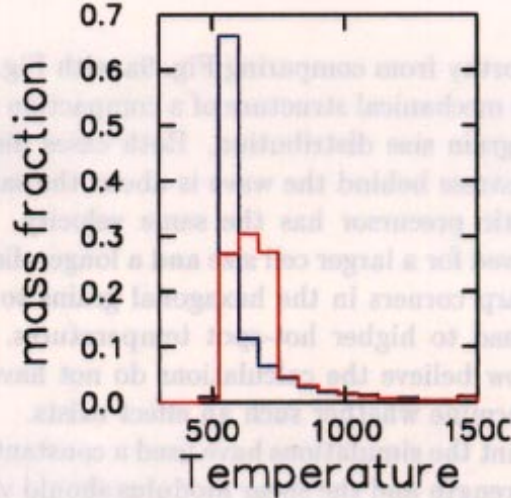


Figure 28: Effect of lowering yield strength above melting on hot-spot distribution for 1000 m/s piston. Blue is standard case with constant yield strength. Red is case in which yield strength vanishes above melting temperature.

show that the plastic work is not the dominant dissipative mechanism for compaction waves strong enough to cause significant melting. Consequently, the change of the yield strength with melting does not have a significant effect on hot spots.

5.3 Effect of Shear Viscosity

The yield strength and the coefficient of shear viscosity control the amount of dissipation from plastic work and viscous shear heating. In the previous subsection we varied the yield strength. Here, the viscous coefficient is varied in order to get a further idea of how sensitive a compaction wave is to the dissipative mechanism.

All the previous calculations used a linear viscous shear stress

$$\sigma' = \mu \frac{d}{dt} \epsilon' ,$$

where $'$ denotes the deviator, with $\mu = 0.031 \text{ GPa} \cdot \mu\text{s}$ (310 Poise) below melting and $\mu = 1.4 \times 10^{-5} \text{ GPa} \cdot \mu\text{s}$ (0.14 Poise) above melting. Since viscosities of solids (other than polymers) are not well known, to get an idea for the magnitude of the coefficient of shear viscosity, we compare it with the artificial viscosity needed for a shock capturing calculation of a plastic shock in a homogeneous solid. For von Neumann-Richtmeyer artificial viscosity the effective viscous coefficient is given by

$$\mu_{\text{NR}} \propto \rho \ell (\mu_1 c + \mu_2 \Delta u) ,$$

where ℓ is a length scale usually taken as the cell size. With the flux-limited artificial viscosity scheme we are able to use dimensionless coefficients $\mu_1 = 0.1$ and $\mu_2 = 1.5$. Taking Δu to be one third of the piston velocity and $\ell = 10 \mu\text{m}$, for the 1000 m/s piston, the artificial viscosity is dominated by the μ_2 term, and the coefficient is 150 Poise or about half the shear viscosity coefficient below melting. The artificial viscosity coefficient would be smaller for weaker waves driven by lower piston velocities. Finally, we note that for liquids at atmospheric pressure, viscosities are typical in the range of 10^{-3} to 10^{-1} Poise.

The stress profiles, σ_{xx} and σ_{equiv} , of a compaction wave driven by a 1000 m/s piston are shown in Fig. 29 for simulations (mono-dispersed granular bed as in Subsection 5.1) with and without shear viscosity. The profiles

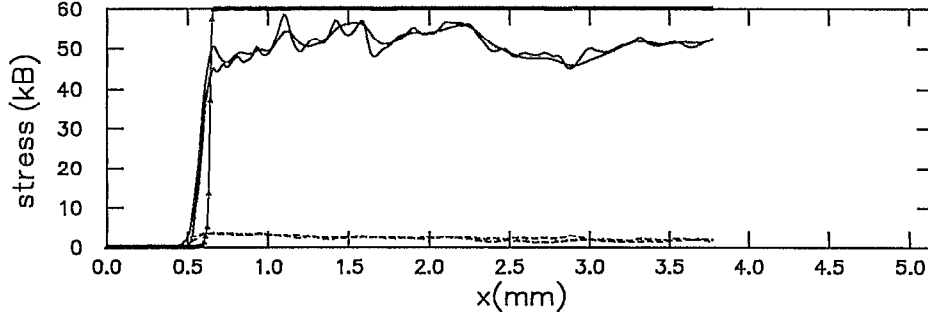


Figure 29: Comparison of compaction wave profiles, σ_{xx} (solid line) and σ_{equiv} (dashed line), for 1000 m/s piston at $t = 1.4 \mu\text{s}$: blue is without shear viscosity and red is with shear viscosity. Black line with symbols is numerical profile for shock in homogeneous solid at time ($0.9 \mu\text{s}$) to match position of wave front and scaled to 60 kb.

for these two cases are nearly the same. Also plotted in the figure is the shock profile for a homogeneous solid. The homogeneous case shows the resolution limited shock width of the simulations. The wave width in the granular bed is about 1 grain diameter and is several times larger than the numerical resolution. Thus, with the parameters we are using, the grain scale rather than the dissipative mechanism dominates the stress profile when the compaction wave is strong enough to preclude an elastic precursor.

Though the dissipative mechanism hardly affects the stress profiles, it has a significant affect on fluctuations. The temperature distribution with and without shear viscosity is compared in Fig. 30. Surprisingly, the tail of the distribution is larger without shear viscosity. This is because shear viscosity, by smoothing out the velocity field at the wave front, decreases the amount of plastic deformation at grain boundaries and hence the peak plastic work.

The extreme tail of the temperature fluctuations, $T > 1500$, is not shown in Fig. 30. Hot spots of only 1 or 2 cells dominate the extreme tail. Unfortunately, these cannot be distinguished from numerical artifacts. Very likely meaningful temperatures will require some sort of smoothing at grain boundaries. Unless the hot spots can be resolved, smoothing runs the risk of underestimating the high end of the temperature distribution. For our simulations, half the mass of a grain is within 2 cells of the grain boundary. Clearly this is not sufficient resolution to determine accurately the tempera-

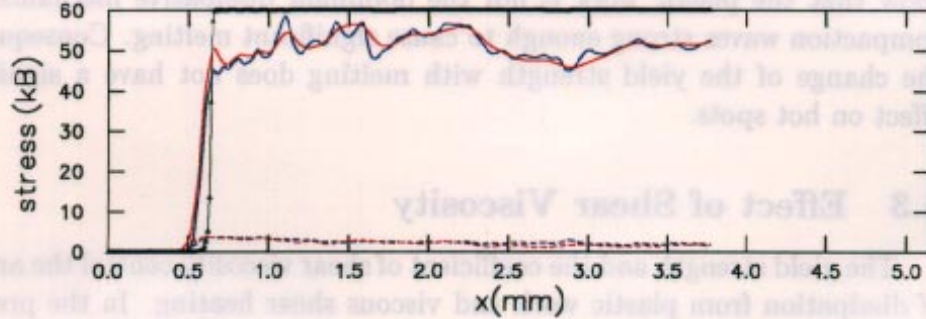


Figure 29: Comparison of compaction wave profiles, σ_{xx} (solid line) and σ_{equiv} (dashed line), for 1000 m/s piston at $t = 1.4 \mu s$: blue is without shear viscosity and red is with shear viscosity. Black line with symbols is numerical profile for shock in homogeneous solid at time ($0.9 \mu s$) to match position of wave front and scaled to 60 kb.

for these two cases are nearly the same. Also plotted in the figure is the shock profile for a homogeneous solid. The homogeneous case shows the resolution limited shock width of the simulations. The wave width in the granular bed is about 1 grain diameter and is several times larger than the numerical resolution. Thus, with the parameters we are using, the grain scale rather than the dissipative mechanism dominates the stress profile when the compaction wave is strong enough to preclude an elastic precursor.

Though the dissipative mechanism hardly affects the stress profiles, it has a significant affect on fluctuations. The temperature distribution with and without shear viscosity is compared in Fig. 30. Surprisingly, the tail of the distribution is larger without shear viscosity. This is because shear viscosity, by smoothing out the velocity field at the wave front, decreases the amount of plastic deformation at grain boundaries and hence the peak plastic work.

The extreme tail of the temperature fluctuations, $T > 1500$, is not shown in Fig. 30. Hot spots of only 1 or 2 cells dominate the extreme tail. Unfortunately, these cannot be distinguished from numerical artifacts. Very likely meaningful temperatures will require some sort of smoothing at grain boundaries. Unless the hot spots can be resolved, smoothing runs the risk of underestimating the high end of the temperature distribution. For our simulations, half the mass of a grain is within 2 cells of the grain boundary. Clearly this is not sufficient resolution to determine accurately the tempera-

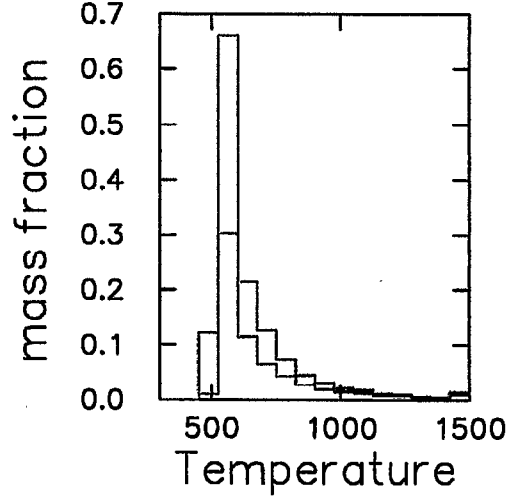


Figure 30: Comparison of shear viscosity on temperature fluctuations behind compaction wave for 1000 m/s piston at $t = 1.4 \mu\text{s}$: blue is without shear viscosity and red is with shear viscosity.

ture fluctuations.

The Arrhenius reaction rate, which we used to compute hot spot induction time in Fig. 4, is extremely temperature sensitive. Consequently, even if the extreme tail of the temperature distribution corresponds to a very small mass, it can have a significant effect on the mass-averaged reaction rate. The sensitivity of the reaction rate together with the limited resolution, which results in temperature inaccuracies, prevent us from presenting meaningful quantitative results on how the temperature fluctuations affect the mass-averaged reaction rate.

With larger values of the shear viscosity, the compaction wave width begins to increase. To see this effect we tripled the shear viscosity to 1000 Poise. A comparison of the stress profiles for compaction wave in the mono-dispersed bed driven by a 500 m/s piston are shown in Fig. 31. The wave width is only slightly larger. This implies that the viscosity would have to be very large for the viscous length scale to dominate the length scale from the granular heterogeneities. The larger viscosity also affects the hot spots. A comparison of the temperature distribution is shown in Fig. 32. We see that the tail of the distribution increases with viscosity.

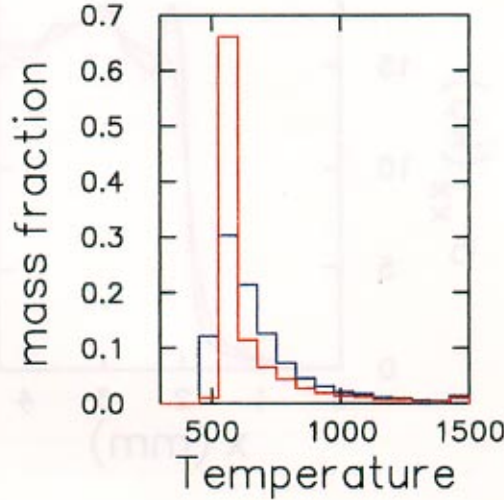


Figure 30: Comparison of shear viscosity on temperature fluctuations behind compaction wave for 1000 m/s piston at $t = 1.4 \mu\text{s}$: blue is without shear viscosity and red is with shear viscosity.

ture fluctuations.

The Arrhenius reaction rate, which we used to compute hot spot induction time in Fig. 4, is extremely temperature sensitive. Consequently, even if the extreme tail of the temperature distribution corresponds to a very small mass, it can have a significant effect on the mass-averaged reaction rate. The sensitivity of the reaction rate together with the limited resolution, which results in temperature inaccuracies, prevent us from presenting meaningful quantitative results on how the temperature fluctuations affect the mass-averaged reaction rate.

With larger values of the shear viscosity, the compaction wave width begins to increase. To see this effect we tripled the shear viscosity to 1000 Poise. A comparison of the stress profiles for compaction wave in the mono-dispersed bed driven by a 500 m/s piston are shown in Fig. 31. The wave width is only slightly larger. This implies that the viscosity would have to be very large for the viscous length scale to dominate the length scale from the granular heterogeneities. The larger viscosity also affects the hot spots. A comparison of the temperature distribution is shown in Fig. 32. We see that the tail of the distribution increases with viscosity.

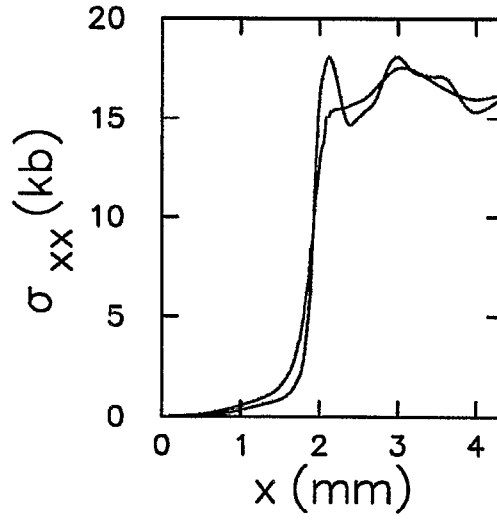


Figure 31: Comparison of compaction wave profiles, σ_{xx} for 500 m/s piston at $t = 1.6 \mu\text{s}$: blue is standard shear viscosity and red is high shear viscosity.

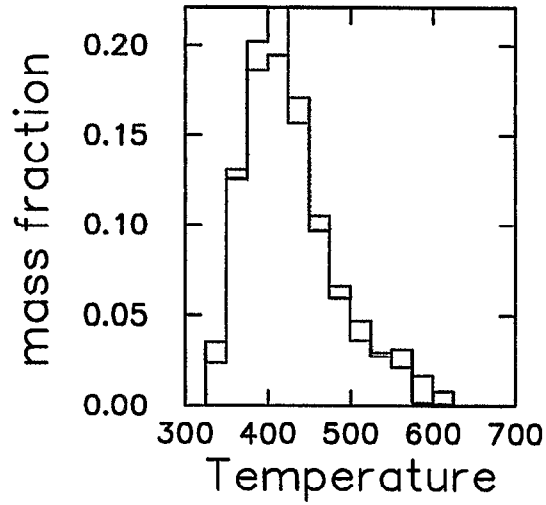


Figure 32: Comparison of temperature fluctuations behind compaction wave for 500 m/s piston at $t = 1.6 \mu\text{s}$: blue is standard shear viscosity and red is high shear viscosity.

5.4 Effect of Grain Distribution

To check the effect the grain distribution has on a compaction wave we compared simulations with a random and a regular mono-dispersed granular bed. The regular bed was generated from a closed-packed array of circles by randomly decreasing the radius of 90% of the circles by up to 10%. This procedure resulted in granular beds with nearly the same porosity: 17.6% for the regular array and 18.6% for the random array.

The stress profiles are shown Fig. 33. The compaction wave in the bed with the larger initial porosity has a slower wave speed. The times are selected such that the plastic wave is at the same position. The precursor is slightly weaker for the regular array. In principle, the way the regular array is constructed the grains are not touching, and the precursor should disappear. However, the spacing between grains is within one cell, and hence the grains are coupled due to the limited numerical resolution. A loosely packed granular bed, in which there are fewer contacts per grain, would have a similar effect on the precursor.

The temperature distributions are compared in Fig. 34. The tail of the distribution is larger for the bed with the random packing. This is because a grain in the regular array has more contacts, which lowers the stress concentrations, and hence lowers the peak plastic work.

This comparison again shows that the wave stress is determined by the Hugoniot jump relations, which depend on the porosity. But the hot-spot distribution is sensitive to those aspects of the granular distribution which affect stress concentrations. In addition, the elastic precursor and small amplitude long-wave length stress fluctuations are also affected by the granular distribution.

5.5 Mesh Refinement

The resolution in our simulations is adequate for the stress profiles but not for the hot-spot distribution. Cutting the cell size in half would require that the length of the mesh be reduced by a factor of 2 to 3 in order for the computation to fit within the available memory (128 Mb) on our workstation. With half the distance of run, start-up transients would play a larger role. Moreover, a factor of two increase in resolution is still not sufficient to resolve hot spots and would not provide a test of convergence. For the moment, our confidence in the calculations rests with interpreting the numerical results in

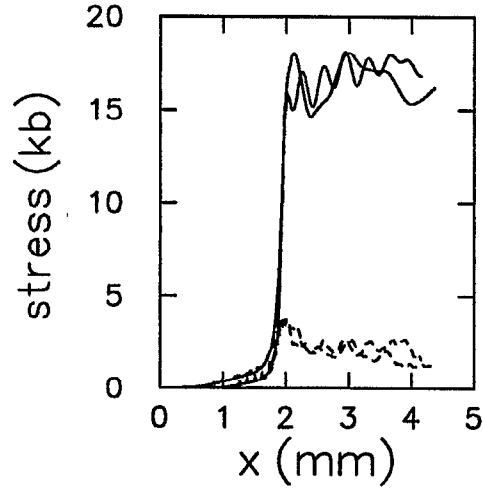


Figure 33: Comparison of stress profiles for 500 m/s piston; blue is mono-dispersed granular bed at $t = 1.6 \mu\text{s}$ and red is modified regular array at $t = 1.4 \mu\text{s}$. Solid lines are σ_{xx} and dashed lines are σ_{equiv} .

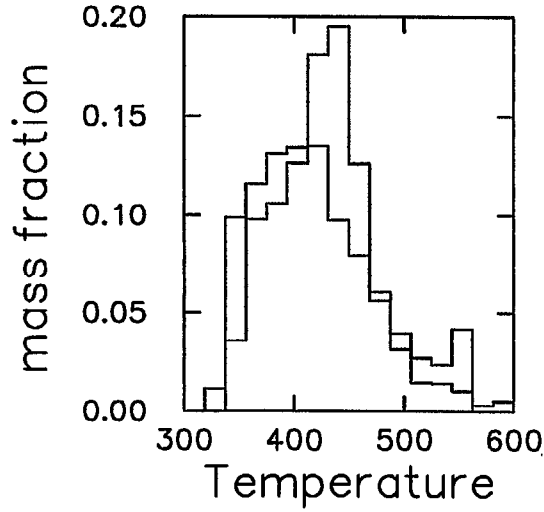


Figure 34: Comparison of temperature distribution behind wave ($3 < x < 4$) driven by 500 m/s piston. Blue is mono-dispersed granular bed at $t = 1.6 \mu\text{s}$ and red is modified regular array at $t = 1.4 \mu\text{s}$.

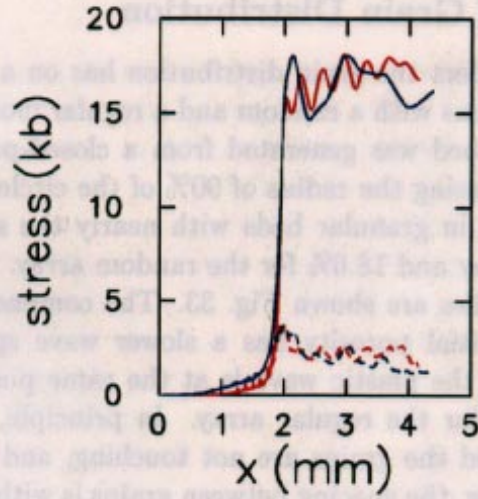


Figure 33: Comparison of stress profiles for 500 m/s piston; blue is mono-dispersed granular bed at $t = 1.6 \mu\text{s}$ and red is modified regular array at $t = 1.4 \mu\text{s}$. Solid lines are σ_{xx} and dashed lines are σ_{equiv} .

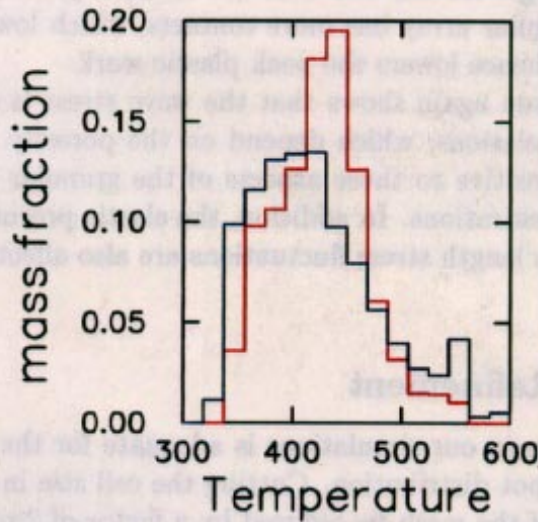


Figure 34: Comparison of temperature distribution behind wave ($3 < x < 4$) driven by 500 m/s piston. Blue is mono-dispersed granular bed at $t = 1.6 \mu\text{s}$ and red is modified regular array at $t = 1.4 \mu\text{s}$.

terms of our physical understanding of the wave structure.

When the ASCI computers and hydrocodes become available, increasing the resolution by a factor of 5 should be possible. This would increase the memory requirement by a factor of 25 and the computational effort by a factor of 125. This “high resolution” would have 70 cells per grain diameter and would give a reasonable chance of resolving dissipation in the vicinity of grain boundaries. In addition, mesh refinement techniques would become possible since the interface cells would represent a small enough fraction of the total number of cells.

For 3-D calculations these more powerful machines would still only allow for the same resolution as we are currently using in 2-D. A medium resolution 3-D calculation would require about the same computational effort as a high resolution 2-D calculation but would require another factor of 5 in memory. Even with the limited resolution, 3-D simulations would give an idea of the effect of dimensionality and possibly suggest how the 2-D simulations could be scaled in order to compare with physical experiments.

6 Homogenized Models

At this point it is natural to ask to what extent homogenized continuum models can reproduce the behavior of compaction waves based on the underlying micro-mechanical properties of a granular bed. The simulations show that mechanical properties, such as wave speed and stress, are insensitive to the dissipative mechanism. The insensitive quantities are determined largely by the constitutive properties of the pure solid and the conservation laws, *i.e.*, the porous Hugoniot locus. Consequently, the simple P - α model, when empirically calibrated to reproduce the volume fraction, is able to determine the state behind a compaction wave.

Continuum models also make predictions for the wave profile. However, the wave profile does depend on dissipative mechanisms, and quantities such as the wave width, or the existence of a precursor can vary between models. The dissipative mechanisms become important for attempts to generalize a model in order to account for the effect of hot spots on the reaction rate. Below we briefly comment on a fluid model and a plasticity model that have been applied to porous materials such as a granular bed.

6.1 Fluid Model

Two-phase fluid like models have been used to study DDT in granular explosives. This is exemplified by the Baer-Nunziato model [30]. Its single-phase limit can be used to describe the compaction of an inert granular bed. In this case the model consists of the conservation equations for fluid flow, Eq. (2), the P - α form for the equation of state

$$P(V, e, \phi) = \phi P_s(\phi V, e) \quad (19)$$

and a rate equation for the volume fraction

$$\frac{d\phi}{dt} = \frac{\phi(1-\phi)}{\mu_c} \left(P_s - \beta(\phi) \right), \quad (20)$$

which enables the pressure to relax towards an equilibrium value. The equilibrium pressure $\beta(\phi)$ is the inverse function of the equilibrium volume fraction in the P - α model. The relaxation rate is controlled by the parameter μ_c , which has dimensions of viscosity. The standard porous Hugoniot locus is a consequence of these equations.

As is typical with relaxation systems, this model has a frozen sound speed and an equilibrium sound speed. The frozen sound speed is just the sound speed of the pure solid, c_s . The equilibrium sound speed c_{eq} is lower than the frozen sound speed and is determined by $\beta(\phi)$ and the solid equation of state $P_s(V_s, e)$. Changes in volume fraction are dissipative with the rate of entropy increase given by

$$T \frac{d\eta}{dt} = \left(P_s - \beta(\phi) \right) V \frac{d\phi}{dt}. \quad (21)$$

As a consequence of the dissipation, the model predicts fully dispersed compaction waves with wave speeds between c_{eq} and c_s , and partly dispersed waves with wave speeds above c_s .

Two other properties of the dynamics of the volume fraction are noteworthy. First, the volume fraction is not solely a function of pressure but is rate dependent. Our simulations, Fig. 16, also show a rate dependence. Second, the time constant for the volume fraction equation is proportional to $\mu_c/(P_s - \beta)$. Consequently the width of a compaction wave decreases with wave strength.

Though the model captures many of the properties of a granular bed, several qualitative features of compaction waves are not in agreement with

our micro-mechanical simulations. These are listed below:

- (i) Weak compaction waves are not steady but spread out in time. This is the result of the plastic work providing excess dissipation compared to that required by the Hugoniot jump relations.
- (ii) For weak compaction waves the average of the components of the stress deviator do not vanish. Thus, a hydrostatic pressure does not adequately characterize the stress.
- (iii) Moderate strength compaction waves display an elastic precursor. The elastic precursor is very dispersed, and the speed of the leading edge lies between the bulk sound speed c_s and the longitudinal sound speed.
- (iv) Since the porosity is determined by the yield strength, it is natural to associate the compaction dissipation in Eq. (21) with the plastic work. However, the compaction work only dominates the dissipation for weak waves. The 500 m/s piston drives a compaction wave with a speed 2.1 km/s, well below the bulk sound speed of 2.65 km/s. Yet the plastic work provides only about half of the dissipation when the hydrodynamic model predicts a fully dispersed wave with all the dissipation from compaction work. Other dissipative mechanisms imply that the wave width is not determined solely by the compaction work.
- (v) The width of a compaction wave does decrease with wave strength but saturates at a value proportional to the grain size. To achieve this effect μ_c would have to increase with pressure.

These discrepancies between the behavior of the hydrostatic model and the underlying micro-mechanical description should not be surprising. Porosity under compressive stress is made possible by material strength. The hydrostatic model crudely accounts for material strength with the configuration pressure $\beta(\phi)$ and the compaction rate equation (20). It can only describe accurately those wave properties which are not sensitive to the details of the dissipation mechanism.

6.2 Plasticity Model

An inherent limitation of the fluid model is that it doesn't account for the tensor character of either the stress or the strain. Experiments in powdered metals show that the mean stress differs for hydrostatic and uniaxial compression [32, Fig. 6]. A simple equilibrium volume fraction or configuration pressure can not account for such a difference. In addition, for quasi-static compression experiments [15], which are used to measure the configuration

pressure of a granular bed, wall friction is a 40% effect. This indicates that shear stress is significant and should not be neglected.

The stress-strain plots in Figs. 21-23 suggest that the average behavior of a granular bed might be described with a plasticity model. This has been proposed before, see for example [33, 34, 35, 36, 32]. One reason it hasn't been pursued is the lack of experimental data. Compaction wave experiments typically measure the velocity or the longitudinal component of stress σ_{xx} . It is a difficult experimental challenge to obtain data on the stress deviator in a compaction wave profile.

Plasticity models have been developed for metals and typically assume that the plastic strain is volume preserving. This assumption is based on the underlying microscopic view that crystal plasticity is due to the motion of dislocations. The underlying structure of a granular material changes the plastic behavior. A plasticity model with the yield strength depending on pressure and an associative-flow rule would give rise to a plastic strain with a volumetric component [32]. The volumetric component of the plastic strain can be associated with the change in porosity. Thus, the flow rule for the plastic strain would replace the rate equation for the volume fraction in the fluid model, Eq. (20).

Such a plasticity model, which has been developed in the field of soil mechanics, is known as critical state theory. It has been applied to quasi-static deformations of granular materials [37] and to shear flow of a granular material approximated by a rigid-perfectly plastic material [38]. For the latter case, there are unstable flow regimes leading to shear layers. Dissipation along a shear layer resulting from such a mechanism is a potential source of hot spots. This would be worth pursuing since for an explosive it is important to understand all ignition mechanisms in order to predict with confidence the outcome of an accident scenario.

However, it should be noted that there are two significant complications with applying a plasticity model to compaction waves in a porous material. First, there is no conservation law for the plastic strain, and the porosity is not determined by a simple algebraic equation. Consequently, the Hugoniot jump conditions are not sufficient for determining the end state of a compaction wave. Instead one would have to resolve the wave profile for partly compacted waves. The Hugoniot conditions would be sufficient for strong fully compacted waves. The second complication stems from the relaxation of the stress deviators shown in Figs. 11 and 21. Possibly this could be accounted for with a strain softening, *i.e.*, lowering the yield strength with plastic strain.

Micro-mechanical simulations are a means of obtaining further guidance for developing better constitutive models of heterogeneous materials. The stress profile and fluctuations of a compaction wave are determined by the dissipative mechanisms. The dissipative mechanisms depend on the underlying micro-structure. Since fluctuations are important for reactive flow, reactive flow is more sensitive to the micro-structure than is the flow of an inert material.

7 Summary and Conclusions

Compared to a homogeneous material, granular heterogeneities have several effects on a shock wave. For inert materials, the dominant effect is the additional degree of freedom associated with the solid volume fraction. This can be described with simple fluid like models, such as the P - α model or the two-phase Baer-Nunziato model. These models assume a hydrostatic stress, and postulate an equilibrium volume fraction or a configuration pressure to account for the effect of material strength that enables a granular bed to support a non-zero porosity under compressive stress. This allows the models to describe the volume change associated with the crush-up of the pores in a compaction wave.

The end state of a compaction wave is largely determined by the porous Hugoniot locus. Fluid like models are adequate when the details of the wave structure are not of interest. The structure of the wave, such as the wave width or an elastic precursor, depends on the dissipative mechanism. Our micro-mechanical simulations are aimed at describing the wave profile.

A major effect of heterogeneities, of importance for the initiation of an explosive, is the temperature fluctuations or hot-spot distribution. The hot-spot distribution is sensitive to the dissipative mechanism. Our compaction wave simulations have three dissipative mechanisms; plastic work, shear viscosity and artificial bulk viscosity. Plastic work results from the deformation of grains needed to decrease the porosity. Shear viscosity mocks up the effect of friction between grains and along closed cracks. Artificial viscosity is needed for numerical stability of strong shocks. For the range of piston velocities we studied, the dispersive effects of the heterogeneities spread the compaction wave by a much larger amount than would be generated by the artificial viscosity in a homogeneous material.

The yield strength determines the crush-up pressure needed to fully compact a granular bed. For HMX, the yield strength inferred from hard-

ness measurements is 0.13 GPa and from wave profiles in a single crystal is 0.3 GPa. Very likely the yield strength is affected by work hardening. This is an important quantity that should be experimentally determined more accurately.

For weak partly compacted waves, plastic work is the dominate dissipation mechanism in the wave profile. Plastic work is concentrated around the contact surfaces between grains and leads to hot spots. For HMX, at full compaction the plastic work is sufficient to bring hot spots up to the melting temperature. It is important to note that the melting temperature increases with pressure and that the Arrhenius reaction rate is much larger for the liquid phase than for the solid phase.

The simulations show that a 500 m/s piston gives rise to hot spots with temperatures upwards of 600 K. These hot spots would have an induction time on the order of 100 μ s. This compares with a bulk temperature of only 425 K, which is too low for appreciable burning to occur. Plastic work is limited by melting. Other dissipative mechanisms are the dominate source for hot spots above the melting temperature. Very likely hydrodynamic void collapse, studied in connection with shock initiation [2, Sec. 3.3], becomes the dominate source of hot spots as the wave strength is increased.

Though our simulations display temperature fluctuations, the limited resolution prevents us from presenting quantitative results. The qualitative trends are physically plausible, and the hot spots are in the regime (maybe slightly low) that would result in burning and affect ignition sensitivity. Computations on the more powerful ASCI computers should enable hot spots to be resolved and allow for quantitative results on the temperature distribution. This is a prerequisite for including burn in the simulations. Also, the ASCI computers should allow for 3-D simulations, which are necessary to understand the effect of dimensionality needed to compare high resolution 2-D simulations with physical experiments.

Even with adequate resolution, a critical aspect of the simulations is the dissipative mechanisms included in the numerical model. One uncertainty arises from the coefficient of shear viscosity used to mock up frictional heating at grain interfaces. Properly accounting for frictional heating would require a good treatment of shear layers. In addition, the effect of crystal orientation and rate dependent plasticity could be incorporated. Rate dependent plasticity would introduce another time scale and could lead to a grain size dependence of the hot-spot distribution for weak waves resulting from the plastic work.

The long-term goal of this work is to develop an improved burn model for continuum codes. This is our first attempt at using micro-mechanical simulations to determine the hot-spot distribution from compaction waves and how it is affected by wave strength. Hot spots are sub-grain in size and require high resolution simulations. In addition, fluctuations are sensitive to the dissipative mechanism. Though plastic work is clearly important for weak waves, other dissipative mechanisms may also be important. Micro-mechanical simulations can also provide guidance for developing constitutive models of heterogeneous materials.

Acknowledgments

We thank David Benson, Univ. of Calif. San Diego, for making his COMADREJA code available to us. Discussions with Paul Conley, Univ. of Calif. San Diego, on compaction waves have been mutually beneficial. Comments from Charles Mader, retired Fellow of LANL, have been helpful.

Appendix I: Mie-Grüneisen Equation of State

The Mie-Grüneisen equation of state has the form

$$P(V, e) = P_{\text{ref}}(V) + \frac{\Gamma}{V} (e - e_{\text{ref}}(V)) \quad (22)$$

where Γ is the Grüneisen coefficient. Assuming that Γ is independent of e amounts to linearizing the pressure in e about the reference curve.

For many solids, high pressure data is available for the principal Hugoniot. Consequently, the principal Hugoniot is frequently chosen as the reference curve. It follows from the shock jump conditions:

$$\frac{u_p}{u_s} = 1 - \frac{V}{V_0}, \quad (23)$$

$$P_h = P_0 + \rho_0 u_p u_s, \quad (24)$$

$$e_h = \frac{1}{2} (P_h + P_0) \cdot (V_0 - V), \quad (25)$$

where u_s is the shock velocity and u_p is the particle velocity. These jump conditions together with a $u_s(u_p)$ relation determine $P_h(V)$ and $e_h(V)$. Frequently, a linear relation, $u_s = c_0 + s u_p$, is a good approximation for pressures below the bulk modulus, $\rho_0 c_0^2$.

The temperature and energy on the initial isentrope are determined by integrating the ODEs

$$\frac{d}{dV} \begin{pmatrix} T \\ e \end{pmatrix} = - \begin{pmatrix} \frac{\Gamma T}{V} \\ P \end{pmatrix} . \quad (26)$$

The temperature as a function of V and e is based on a constant specific heat

$$T(V, e) = T_s(V) + \frac{e - e_s(V)}{C_V} . \quad (27)$$

Finally, the thermal effect of melting can be incorporated by modifying the specific energy

$$\tilde{e} = \begin{cases} e - \max[Q, C_v \cdot (T - T_m)] & \text{if } T > T_m, \\ e & \text{otherwise,} \end{cases} \quad (28)$$

where T_m is the melting temperature and Q is the latent heat of melting. The pressure and temperature are then recomputed with e replace by \tilde{e} in Eqs. (22) and (27). The change in volume associated with melting is neglected.

Appendix II: Elastic-Plastic Model

The strength model determines the stress deviator $\boldsymbol{\sigma}' = \boldsymbol{\sigma} - \frac{1}{3}\text{Tr}(\boldsymbol{\sigma})\mathbf{I}$. In the range of interest we assume that (i) the stress depends only on the elastic strain, (ii) the material is isotropic, and (iii) the shear modulus is approximately constant. The stress rate can be expressed as

$$\frac{d}{dt}\boldsymbol{\sigma}' = 2G \left(\frac{d}{dt}\boldsymbol{\epsilon}' - \frac{d}{dt}\boldsymbol{\epsilon}'_p \right) , \quad (29)$$

where $\boldsymbol{\epsilon}$ is the total strain and $\boldsymbol{\epsilon}_p$ is the plastic strain. The plastic strain rate is based on von Mises yield condition

$$\frac{3}{2} \|\boldsymbol{\sigma}'\|^2 \leq Y^2 , \quad (30)$$

and the associated flow rule

$$\frac{d}{dt}\boldsymbol{\epsilon}'_p = \lambda \boldsymbol{\sigma}' . \quad (31)$$

For rate independent plasticity, the factor λ is determined uniquely from the yield condition Eq. (30).

References

- [1] F. P. Bowden and Y. D. Yoffe. *Initiation and Growth of Explosion in Liquids and Solids*. Cambridge Univ. Press, Cambridge, UK, 1952.
- [2] C. L. Mader. *Numerical Modeling of Explosives and Propellants*. CRC Press, Boca Raton, FL, second edition, 1998.
- [3] R. E. Setchell. Effects of precursor waves in shock initiation of granular explosives. *Combustion and Flame*, 54:171–182, 1983.
- [4] A. W. Campbell and J. R. Travis. The shock desensitization of PBX-9404 and composition B-3. In *Eighth (International) Symposium on Detonation, Albuquerque, NM, July. 15, 1985*, pages 1057–1067. Naval Surface Weapons Center, White Oak, Silver Spring, MD, 1985.
- [5] E. L. Lee and C. M. Tarver. Phenomenological model of shock initiation in heterogeneous explosives. *Phys. Fluids*, 23:2362–2372, 1980.
- [6] J. N. Johnson, P. K. Tang, and C. A. Forest. Shock-wave initiation of heterogeneous reactive solids. *J. Appl. Phys.*, 57:4323–4334, 1985.
- [7] J. E. Field, N. K. Bourne, S. J. P. Palmer, and S. M. Walley. Hot-spot ignition mechanisms for explosives and propellants. *Phil. Trans. Roy. Soc. London*, A 339:269–283, 1992.
- [8] J. M. McAfee, B. Asay, W. Campbell, and J. B. Ramsay. Deflagration to detonation in granular HMX. In *Ninth (International) Symposium on Detonation, Portland, OR, Aug. 28, 1989*, pages 265–279. OCNR 113291-7, Office of the Chief of Naval Research, Arlington, VA, 1989.
- [9] S. A. Sheffield, R. L. Gustavsen, and M. U. Anderson. Shock loading of porous high explosives. In L. Davison, Y. Horie, and M. Shahinpoor, editors, *High-pressure shock compression of solids IV: response of highly porous solids to shock compression*, chapter 2, pages 23–61. Springer-Verlag, New York, 1997.
- [10] D. J. Benson. The numerical simulation of dynamic compaction of powders. In L. Davison, Y. Horie, and M. Shahinpoor, editors, *High-pressure shock compression of solids IV: response of highly porous solids*

to shock compression, chapter 9, pages 233–255. Springer-Verlag, New York, 1997.

- [11] D. J. Benson, V. F. Nesterenko, F. Jonsdottir, and M. A. Meyers. Quasi-static and dynamic regimes of granular material deformation under impulse loading. *J. Mech. Phys. Solids*, 45:1955–1999, 1997.
- [12] R. L. Gustavsen and S. A. Sheffield. Unreacted Hugoniot for porous and liquid explosives. In *High-Pressure Science and Technology - 1993, Proceedings of the American Physical Society Topical Group on Shock Compression of Condensed Matter, Colorado Spgs, CO*, pages 1393–1396. American Institute of Physics, NY, 1994.
- [13] Jean-Paul Poirier. *Introduction to the Physics of the Earth's Interior*. Cambridge Univ. Press, Cambridge, UK, 1991.
- [14] J. J. Dick, A. R. Martinez, and R. S. Hixson. Plane impact response of PBX 9501 and its components below 2 GPa. Technical Report LA-13426-MS, Los Alamos National Lab., 1998.
- [15] W. L. Elban and M. A. Chiarito. Quasi-static compaction study of coarse HMX explosive. *Powder Technology*, 46:181–193, 1986.
- [16] S. J. P. Palmer and J. E. Field. The deformation and fracture of β -HMX. *Proc. Roy. Soc. London, A* 383:399–407, 1982.
- [17] D. J. Benson. A new two-dimensional flux-limited shock viscosity for impact calculations. *Computer Methods in Applied Mechanics and Engineering*, 93:39–95, 1991.
- [18] W. Herrmann. Constitutive equation for the dynamic compaction of ductile porous material. *J. Applied Phys.*, 40:2490–2499, 1969.
- [19] M. Carroll and A. C. Holt. Suggested modification of the P - α model for porous materials. *J. Applied Phys.*, 43:759–761, 1972.
- [20] T. Boddington. The growth and decay of hotspots. In *Ninth (International) Symposium on Combustion, Ithaca, NY, Aug. 27, 1962*, pages 287–293. Academic Press, NY, 1963.
- [21] J. L. Lubkin. Contact problems. In W. Flügge, editor, *Handbook of Engineering Mechanics*, Chapter 42. McGraw-Hill, NY, 1962.

- [22] D. A. Hills, D. Nowell, and A. Sackfield. *Mechanics of Elastic Contacts*, Chapter 7. Butterworth-Heinemann, Oxford, UK, 1993.
- [23] H. Deresiewicz. Mechanics of granular matter. In *Advances in Applied Mechanics V*, pages 233–306. Academic Press, San Diego, CA, 1958.
- [24] O. J. Schwarz, Y. Horie, and M. Shearer. Discrete element investigation of stress fluctuation in granular flow at high strain rates. *Phys. Rev. E*, 57:2053–2061, 1998.
- [25] D. J. Benson. A mixture theory for contact in multi-material Eulerian formulations. *Computer Methods in Applied Mechanics and Engineering*, 140:59–86, 1997.
- [26] S. N. Coppersmith, C.-H. Liu, S. Majumdar, O. Narayan, and T. A. Witten. Model for force fluctuations in bead packs. *Phys. Rev. E*, 53:4673–4685, 1996.
- [27] L. A. Merzhievsky and A. V. Tyagelsky. Modeling of dynamic compression of porous iron. *Combustion, Explosion and Shock Waves*, 30:522–530, 1994. Translation from *Fizika Goreniya i Vzryva* **30** (4), 124–133.
- [28] L. A. Merzhievsky and A. V. Tyagelsky. Modeling of shock compression of porous media. In *Shock Compression of Condensed Matter – 1995, Proceedings of the American Physical Society Topical Group on Shock Compression of Condensed Matter, Seattle, WA*, pages 303–306. American Institute of Physics, NY, 1995.
- [29] J. M. Walsh and R. H. Christian. Equation of state of metals from shock wave measurements. *Phys. Rev.*, 97:1544–1556, 1955.
- [30] M. R. Baer and J. W. Nunziato. A two-phase mixture theory for the deflagration-to-detonation transition in reactive granular materials. *Int. J. Multiphase Flow*, 12:861–889, 1986.
- [31] V. K. Mohan, V. C. J. Bhasu, and J. E. Field. Role of adiabatic shear bands in initiation of explosives by drop-weight impact. In *Ninth (International) Symposium on Detonation, Portland, OR, Aug. 28, 1989*, pages 1276–1283. OCNR 113291-7, Office of the Chief of Naval Research, Arlington, VA, 1989.

- [32] J. W. Swegle. Constitutive equation for porous materials with strength. *J. Applied Phys.*, 51:2574–2580, 1980.
- [33] H. A. Kuhn and C. L. Downey. Deformation characteristics and plasticity theory of sintered powder materials. *Int. J. Powder Metallurgy*, 7:15–25, 1971.
- [34] R. J. Green. A plasticity theory for porous solids. *Int. J. Mech. Sci.*, 14:215–224, 1972.
- [35] S. Shima and M. Oyane. Plasticity theory for porous metals. *Int. J. Mech. Sci.*, 18:285–291, 1976.
- [36] J. K. Dienes. A high-pressure kinematic hardening model for rock and soils. *Journal of Geophysical Research*, 80:3749–3754, 1975.
- [37] I. F. Collins. The mathematical structure of the equations for quasi-static plane strain deformation of granular materials. In D. D. Joseph and D. G. Schaeffer, editors, *Two Phase Flows and Waves*, IMA vol. 26, pages 30–44. Springer-Verlag, NY, 1990.
- [38] E. B. Pitman and D. G. Schaeffer. Stability of time dependent compressible granular flow in two dimensions. *Comm. Pure and Appl. Math.*, 42:421–447, 1987.

This report has been reproduced directly from the best available copy.

It is available to DOE and DOE contractors from the Office of Scientific and Technical Information, P.O. Box 62, Oak Ridge, TN 37831. Prices are available from (423) 576-8401. <http://www.doe.gov/bridge>

It is available to the public from the National Technical Information Service, US Department of Commerce, 5285 Port Royal Rd., Springfield, VA 22616, (800) 553-6847.

